공학박사 학위논문

Synthesis and Application of Iron Oxide Nanoparticle Based Multifunctional Nanomaterials for Precision Cancer Imaging

산화철 나노입자 기반 다기능성 나노물질의 제조와 정밀 암 영상화 응용에 관한 연구

2019 년 8 월

서울대학교 융합과학기술대학원

융합과학부 나노융합전공

이 채 동

Abstract

Synthesis and Application of Iron Oxide Nanoparticle Based Multifunctional Nanomaterials for Precision Cancer Imaging

Chaedong Lee

Program in Nano Science and Technology

Graduate School of Convergence Science & Technology

Seoul National University

Tumor microenvironment, a sophisticated system consisting of various peripheral cells and cancer-related factors as well as cancer cells, is an emerging key issue in diagnosis and treatment of cancer. Therefore, the development of multimodal imaging contrast agent designed to help understand fundamental aspects of the tumor microenvironment is becoming more important. This dissertation covers novel synthesis and

surface modification process of iron oxide-based multimodal nanoprobes for precision imaging of tumor microenvironment.

In the first part (Chapter 2), the synthetic process of near-infrared (NIR) fluorescent silica-coated superparamagnetic iron oxide nanoparticles (NF-SIONs) and tumor-associated macrophage-specific localization in orthotopic glioblastoma model was demonstrated. NF-SIONs was synthesized via two-step silanization process and fluorescent dye (Cy 5.5)-labeled aminopropyl triethoxysilane (APTES) and polyethylene glycol (PEG)-silane were simultaneously introduced to oleic acid-capped iron oxide nanoparticle via reverse microemulsion method. NF-SIONs showed excellent physicochemical properties and biocompatibility. Immunofluorescence analysis revealed that the administered NF-SIONs exhibited a high uptake in tumor-associated immune cells (monocytes/macrophages/microglia) over cancer cells and brain parenchymal cells.

In the second part (Chapter 3), multi-functionalization of polyethylene glycol (PEG)-capped iron oxide nanoparticle through the introduction of branched ligand was demonstrated. Fluorescent dye and Translocator protein 18 kDa (TSPO, known as GBM biomarker)-targeting compound (CB 235) with NHS-ester terminals were able to bind simultaneously

onto amine binding sites contained in the branched ligand. TSPO-specific behavior was evaluated by confirming localization of the nanoparticles upon administration of competitive inhibitors at tumor-adjacent sites.

In summary, the synthesis and tumor-imaging applications of functionalized iron oxide nanoparticles were studied via systematic immunofluorescence analyses among the tumor-bearing mouse models. The results of this study are expected to contribute to the improved treatment of intractable cancers.

Keywords: Iron oxide nanoparticle, fluorescence labeling, branched ligand, tumor microenvironment, tumor-associated macrophages, multimodal cancer imaging

Student Number: 2012-22451

Contents

List of Figures

List of Tables

Chapter 1.

Introduction

1.1. Cancer nanomedicine

The development of nanotechnology over the past few decades has enabled revolutionary improvement of physicochemical properties of various materials. Based on precise control at the nano level, such as handling biomaterials such as proteins and DNA as well as conventional polymers and inorganic substances, the nanotechnology has become a pivotal role to overcome technical problems in various fields such as electronics, communication, materials, energy and biomedical fields [1].

Nanomedicine is an interdisciplinary approach that helps to diagnose and treat diseases or repair damaged tissues based on nano-sized particle synthesis and processing techniques. The application of nanomedicine extends to diverse fields such as nano-biosensing, bioimaging, nano-drug delivery system, and nano-tissue engineering, and is considered to be as a breakthrough technology for effective treatment of various intractable diseases such as cancer, dementia, cardiovascular disease, and arthritis (**Figure 1.1**) [2].

Cancer is one of the leading causes of death in South Korea, and its incidence has been increasing for last 20 years, due to diverse and yet unclear causes such as external infection and genetic factors as well as life patterns and eating habits [3]. Since successful cancer treatment is

closely related to initial diagnosis, collaborative researches in the academic and medical fields are actively conducted for the precise diagnosis and effective cancer therapy. Current clinical cancer treatment accompanies discomfort of patients due to invasive biopsy and a variety of side effects and risk of recurrence even after surgical operation and chemo/radiotherapy of the tumor. Thus, the development of multifunctional nanomedicine for patient-friendly and efficient tumor therapy is a major stream of cancer nanomedicine research.

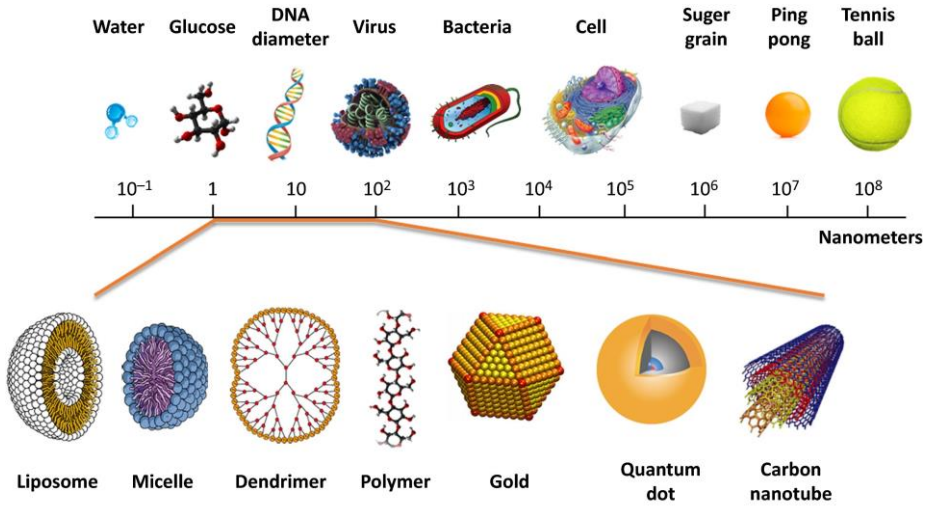

Figure 1.1 Representative objects of various sizes and materials in nanoscale. (from Ref. [4], J. K. L. Wong, R. Mohseni, A. A. Hamidieh, R. E. MacLaren, N. Habib, and A. M. Seifalian, Trends Biotechnol. **35**, 434 (2017))

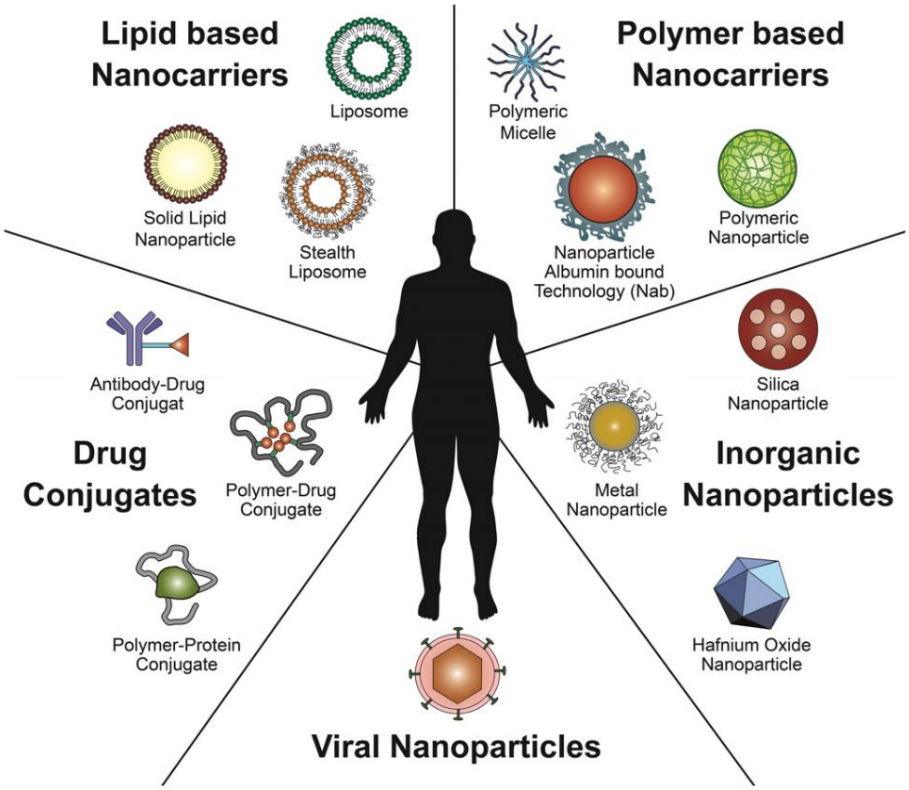

Figure 1.2 Schematic illustration of various nanotherapeutic platforms in cancer nanomedicine. (reproduced from Ref. [2], A. Wicki, D. Witzigmann, V. Balasubramanian, and J. Huwyler, J. Control. Release **200**, 138 (2015))

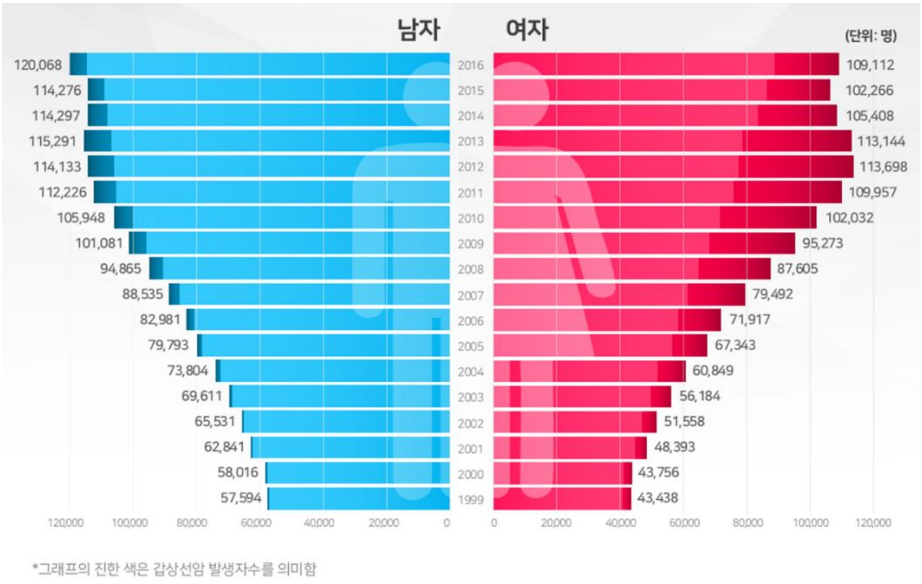

Figure 1.3 Number of cancer cases by sex and year. (source from National Cancer Center, 2016)

Type of Cancer	Treatment	Tumor Control	Adverse Effects
Glioblastoma [5]	Temozolomide	Median survival 14.6 mo. Death in 73.5% by 2 yr.	Gr 3/4 nonhematologic toxicity in 31% (fatigue, rashes, infection, nausea, vomiting)
Head and neck: locally advanced, unresectable [6]	Cetuximab	Median survival 49 mo. Death in 45% by 3 yr. Local failures in 53% by 3 yr. Distant metastases in 17% by 3 yr.	Gr 3-5 mucosal toxicity in 56% Gr 3-5 dysphagia in 26% Gr 3-5 dermatitis in 23% Gr 3-5 weight loss in 11%
Head and neck: locally advanced, resected [7]	Cisplatin	Median survival 48 mo. Local failures in 16% Distant metastases in 20%	Gr 4/5 nonhematologic toxicity in 27% (mucositis, pharyngeal/esophageal toxicity, nausea, vomiting, skin toxicity)
Larynx: locally advanced [8]	Cisplatin	Death in 26% by 2 yr. Laryngectomy in 12% by 2 yr. Distant metastases in 8% by 2 yr.	Acute gr 3/4 nonhematologic toxicity in 77% (mucositis, pharyngitis/esophagitis, laryngitis) Dysphagia persisted at 2 yr. in 15%)
Nasopharynx [9]	Chemotherapy	Death in 24% by 3 yr. Local failures in 14% Distant metastases in 15%	Gr 3 or worse toxicity in 76% (stomatitis, nausea, vomiting, hearing loss, weight loss)
Lung: non-small-cell, locally advanced [10,11]	Chemotherapy before irradiation	Medial survival 13.2 mo. Death in 68% by 2 yr. Local failures in 59% Distant metastases in 39%	Acute gr 3-5 toxicity in 52% Late gr 3-5 toxicity in 3%
Esophagus [12]	Chemotherapy	Medial survival 18 mo. Death in 60% by 2 yr. Local failures in 55% Distant metastases in 16%	Acute gr 3-5 toxicity in 71% (treatment-related death due to infection in2%) Late gr3-5 toxicity in 37% (esophageal stricture, perforation, bleeding)
Breast: early, post lumpectomy [13]	Tamoxifen	Death in7% by 5 yr. (2.5% due to breast cancer) Local failures in 3.5% by 8 yr. Distant metastases in 4.5%	Gr 3 fatigue in 1% Gr 3 skin erythema in 1%
Breast: postmastectomy [14]	Chemotherapy	Death in 53% by 20 yr. Local failures in 13% by 20 yr. Distant metastases in 52%	Fatal cardiac toxicity in 1% at 20 yr. Arm edema in 6% Symptomatic pneumonitis in 0.6%
Pancreas: resected [15]	Chemotherapy	Median survival 17 mo. Death in 80% by 5 yr. Local failures in 23% Regional failures in 23% Distant metastases in 75%	Gr 3 or worse nonhematologic toxicity in 58% (diarrhea, stomatitis, nausea, vomiting)
Cervix [16]	Chemotherapy	Death in 27% by 5 yr. Local failures in 19% Distant metastases in 14%	Acute gr 3-5 nonhematologic toxicity in 11% (nausea, vomiting, diarrhea) Late gr3/5 toxicity in 12% (bowel and urinary effects)
Rectum: locally advanced [17]	Chemotherapy	Death in 24% by 5 yr. Local failures in 6% Distant metastases in 36%	Acute gr 3/4 nonhematologic toxicity in 27% Long-term gr 3/4 toxicity in 14%

The scoring systems used varied among the various papers.

Table 1.1 Chemotherapy side effects in various types of cancer. (source from Ref. [18])

1.2. Tumor microenvironment

Tumorigenesis is a complex and dynamic process responsible for tumor growth and metastasis. Such distinguishing features account for tumor complexity like increased proliferative signals, evasion from growth suppressor, resisting apoptosis, unlimited multiplication, stimulating angiogenesis, promoting invasion and metastasis, modulating cells metabolism and evading immune destruction [19]. These features are acquired through cooperation among different cellular and non-cellular elements of tumors defining the tumor microenvironment (TME). TME consists of non-malignant cells of the tumor such as cancer-associated fibroblasts (CAFs), endothelial cells and pericytes composing tumor vasculature, immune and inflammatory cells, bone marrow-derived cells, and the extracellular matrix (ECM) establishing a complex cross-talk with tumor [20]. Embryonic neoplastic cells, in fact, recruit and activate some stromal cells, which in turn activate biological signals that permit cancer cells to invade surrounding normal tissue and to metastasize in a distant organ. Tumor cells metastasizing in a tissue different from original can survive and expand in the normal microenvironment or meet a favorable microenvironment (pre-metastatic niches), positively pre-conditioned before the arrival of

tumoral cells from several conditions such as circulating factors released by primary tumors [21].

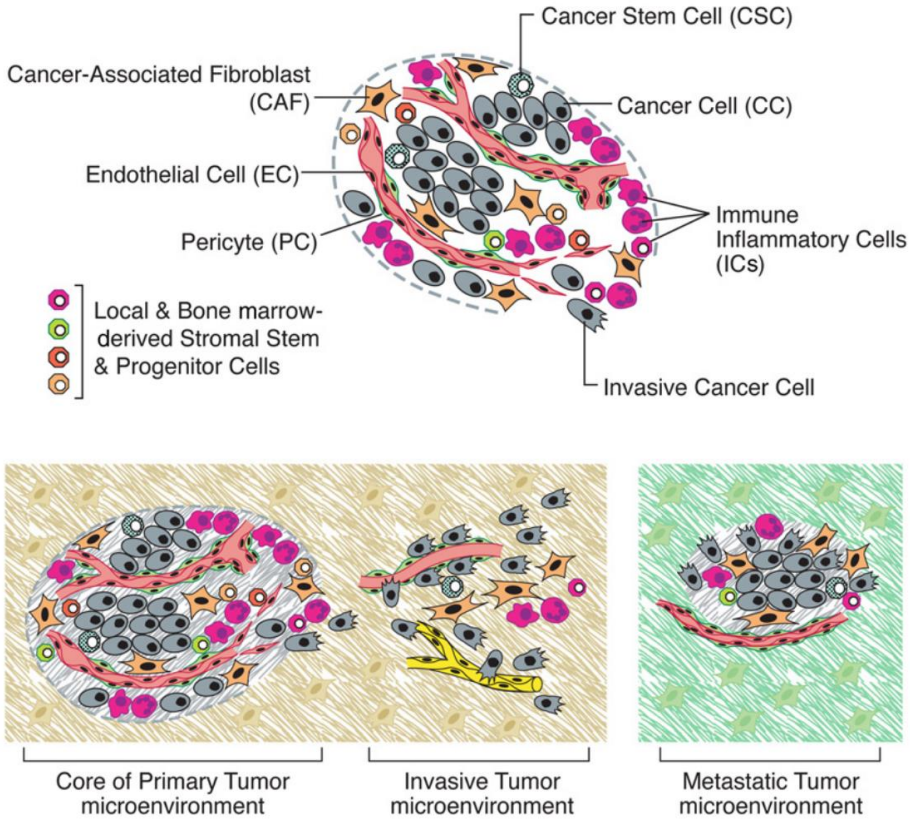

Figure 1.4 Components of the tumor microenvironment and schematic illustration of metastasis process. (reproduced from Ref. [19], D. Hanahan and R. A. Weinberg, Cell **144**, 646 (2011))

1.3. Molecular imaging modalities in cancer imaging

Recent clinical cancer treatments require precise positional information such as tumor location, size, shape, and metastasis. Thus, molecular imaging techniques have been proposed as a means to help understand the anatomical structure, metabolism, and pharmacokinetics of organisms with minimal invasion [22]. The imaging modality used in clinical practice for cancer treatment is positron emission tomography (PET), single photon emission tomography (SPECT), computed tomography (CT), optical imaging and magnetic resonance imaging (MRI) (Figure) [23].

CT is one of the well-known imaging modalities that widely used in clinical practice. The x-ray emission source and the absorption detector are paired to rotate the object around the center of the object and obtain a high-resolution tomographic anatomical image according to the x-ray absorption at each position [24]. Since CT is limited by poor soft tissue contrast, a large amount of contrast agent is needed to obtain an enhanced contrast of soft tissue due to the low sensitivity and remains concerns about side effects.

MRI is a non-invasive imaging technique, which is widely used in medicine. Magnetic resonance images are formed from the nuclear

magnetic resonance (NMR) signal, which is generated by certain nuclei (^{1}H, ^{19}F, ^{31}P, and ^{13}C) when subjected to a strong magnetic field and irradiated with radio waves. After excitation by a radiofrequency (RF) pulse, the nuclear magnetization returns to equilibrium via relaxation [25]. MRI provides excellent contrast between the different soft tissues of the body and specialized to image the brain, muscles, the heart, and cancers compared with other medical imaging techniques such as CT or X-rays. Unlike CT scans or traditional X-rays, MRI has advantages in terms of radiation problem and contrast agent dose.

Optical imaging is technic of using fluorescence and bioluminescence which are based on the energy absorption from an external excitation light by a fluorophore (fluorescence imaging) and light generated by a chemiluminescent reaction, respectively. Fluorescence imaging is advantageous in bioanalysis due to its inexpensiveness, high signal-to ratio and excellent temporal and spatial resolution [26]. Since the fluorescence imaging has several limitations for in vivo application such as low penetration depth and autofluorescence problems, recent studies and clinical researches use near-infrared (NIR) fluorescent dyes due to their low tissue absorption and relatively high penetration skin depth.

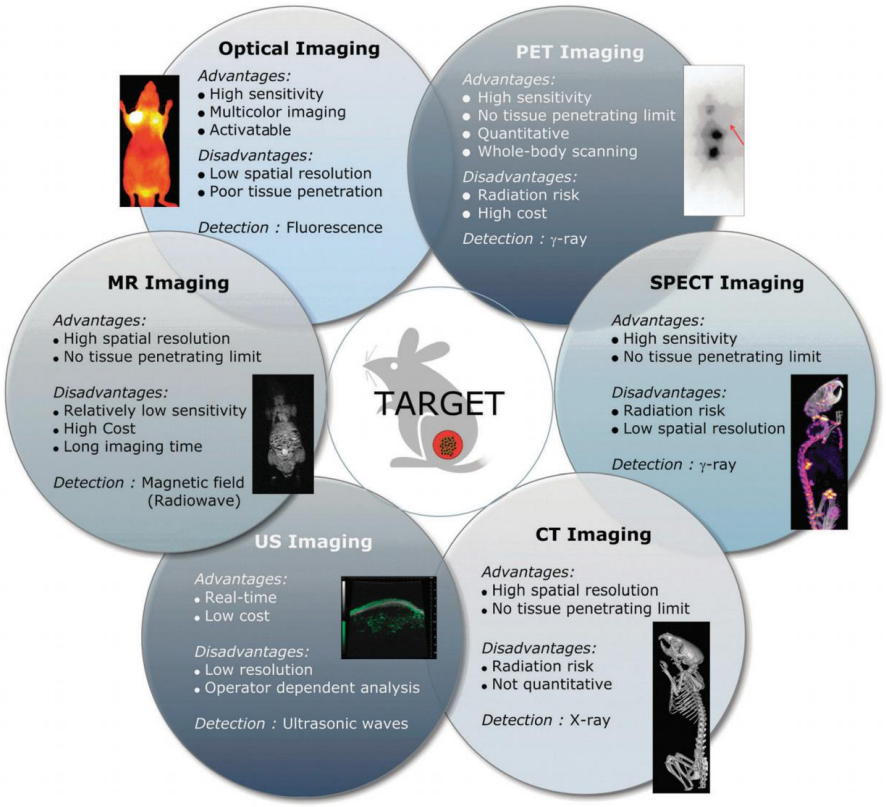

Figure 1.5 Characteristics of imaging modalities currently used in clinical studies. (reproduced from Ref. [23], D. E. Lee, H. Koo, I. C. Sun, J. H. Ryu, K. Kim, and I. C. Kwon, Chem. Soc. Rev. **41**, 2656 (2012))

1.4. Multimodal imaging

Each imaging modality has unique advantages along with intrinsic limitations, such as spatial resolution, penetration depth or insufficient sensitivity, which make it hard to obtain accurate and reliable information from the disease sites [27].

Multimodal imaging is a powerful method that can provide more than two diagnostic information at the same time. Since the operating principles and limitations of each imaging method are different, the improvement of imaging equipment has a limitation in overcoming the disadvantages of each imaging method. For example, PET provides functional information like pharmacokinetics and metabolism with high sensitivity. On the other hand, CT and MRI offer high-resolution images for anatomical information. Therefore, a combination of these different imaging modalities can achieve sensitivity enhancement and higher resolution simultaneously and provide more detailed anatomical or biological information about the target diseases.

Nanoscale multimodal imaging probes with more than two imaging agents have the potential to overcome the limitations of a single imaging modality and to provide more detailed information on the target site through targeted delivery [28,29]. Some inorganic NPs exhibit intrinsic

imaging abilities, such as iron oxide NPs for MR, gold NPs for CT, and quantum dots for optical imaging. These can be combined with different imaging agents by co-encapsulation or conjugation to develop multimodal imaging platforms [30–35].

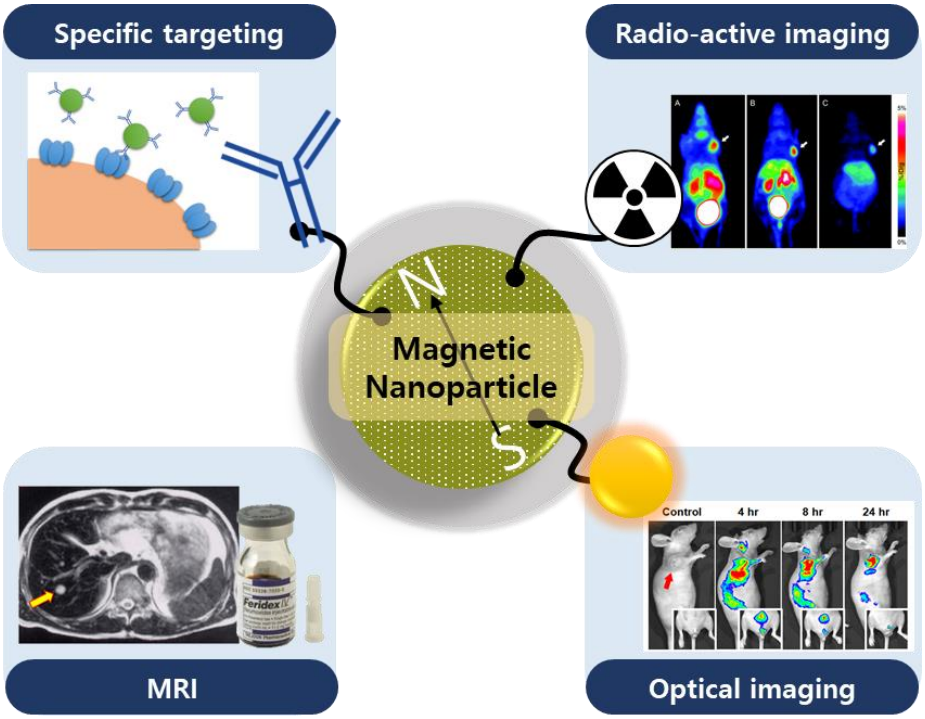

Figure 1.6 Schematic illustration of multifunctional nanoparticle for multimodal imaging and target specificity.

1.5. Research objectives

This thesis is mainly focused on the synthesis and bioimaging application of multifunctional nanoprobes based on iron oxide nanoparticles to improve their fluorescence and dispersion stability for in vivo imaging of several cancer-related factors.

In the first part, the synthesis of fluorescent and magnetic resonance imaging bimodal nanoparticles for targeting tumor-associated macrophages among orthotopic glioblastoma model is discussed. The fluorescent silica-coated iron oxide nanoparticles are synthesized via two-step reverse microemulsion method. The synthesized nanoprobe is administered to a tumor mouse model, and then the migration patterns to various organs and brain tumor sites are compared. In particular, the correlation with tumor-associated macrophages in the vicinity of brain tumors is confirmed by immunofluorescence staining.

In the second part, surface modification and in vivo imaging application of ultra-small iron oxide nanoparticles as a multi-branched platform for fluorescent dye and tumor targeting ligand is discussed. The branched amine ligand is introduced at the surface of the ultra-small iron oxide nanoparticles to support binding sites for NIR fluorescent dye and CB 235 ligand that targets TSPO in the tumor microenvironment. After

confirming the specific uptake of nanoparticles in several cancer cell lines known to be associated with TSPO overexpression, comparative fluorescent imaging study using competitive inhibitor (PK 11195) in a xenograft model are investigated to validate the TSPO targeting characteristics of prepared nanoprobes.

Chapter 2.

Near-Infrared Fluorescent Silica-Coated Iron Oxide Nanoparticle as Tumor-Associated Macrophage Targeting Multimodal Nanoprobe for Surgical Guidance of Glioblastoma

2.1. Introduction

Macrophages are essential components of our innate immune systems. Not only they recognize the antigens and neutralize through phagocytosis, but also macrophages regulate the homeostasis of the cellular environment. Mature macrophages are differentiated from monocytes through polarization process, then exhibit distinctive expressions as their phenotypes, M1 and M2 [36]. While the main the M1 macrophages induce inflammatory responses and tumor necrosis, the M2 macrophages exert anti-inflammatory responses and promote vascularization, which is highly beneficial for growth and metastasis of cancer cells in the tumor microenvironment. Recent studies have shown that tumor-associated macrophages (M2 macrophages) are recognized as important biomarkers in the diagnosis and prognosis of malignant tumors and are thus considered as a potential target for successful tumor therapy [37,38]. Hence, the comprehensive understanding of such tumor-associated macrophages (TAMs) is highly important in successful cancer diagnosis and therapy.

Among the various malignant brain cancers, Glioblastoma multiforme (GBM) is the most frequently encountered disease. Most of GBM patients show extremely low surviving rate (~10%) within 5 years even

after the surgical excision and chemo- or radio-therapies [5,39]. Such severe mortality of GBM is significantly related to the population of accumulated tumor-associated macrophages, comprising 30~50% of whole cells in tumor mass and releasing several factors that promote the glioma growth and invasion [40,41]. In the glioma section of the tumor model, TAMs are distributed along the tumor margin as well as the central part of the tumor [42]. Furthermore, the residual tumor margin after the surgical resection often recurs the GBM, since the determination of tumor boundary is quite subjective and hardly available only by the naked eye during the operations [43].

Fluorescence-guided surgery is an emerging technique for improving oncologic intraoperative procedures. The pre-injected fluorescents agents enhance visualization of tumor margins and help to determine the extent of tumor resection in glioma surgery [44–47]. Traditional small molecule-based fluorophores have been used to provide intraoperative fluorescence guidance in the tumor region for decades, however, they showed the limited circulation time and lack of diagnostic accuracy and specificity due to the diffusion to adjacent interstitial spaces [48,49].

To overcome these problems, nanoparticle-based contrast agents were developed to provide longer blood circulation and target-resident time in

preclinical studies of fluorescence-guided glioma surgery, such as iron oxide nanoparticles [49–51], upconversion nanoparticles [52], and polymer nanoparticles [53–55].

The silica coating method is a well-known process to provide biocompatible and water-dispersible surfaces to nanoparticles which were synthesized in the organic solvent [56–58]. In addition, since the silica shell is optically stable and transparent, it can provide chemically and mechanically stable frameworks for fluorescent dyes by shielding them from external environmental changes [59,60].

In this research, highly water-dispersible and near-infrared fluorescent silica-coated iron oxide nanoparticles (NF-SIONs) was developed as MR/optical combined nanoprobes for *in vivo* cancer imaging. Through successive two-step silica coating process, the hydrophobic iron oxide nanoparticles were converted into nanoparticles with high water dispersibility, strong near-infrared fluorescence properties, and suitable physicochemical properties for biomedical applications. After evaluation of safety and ingestion pattern at the cellular level *in vitro*, *in vivo* biodistribution imaging of intravenously administered nanoparticles was conducted to a mouse model transplanted with tumor cells in the shoulder or brain. In addition, the internalization pattern of nanoparticles

at the tissue level was also examined by immunofluorescence analysis using F4/80, CD11b, and Iba1, which are well-known markers that overexpressed at the tumor-associated macrophages. In addition, the correlation between parenchymal astrocytes and translocated nanoparticles was also investigated by supplementing the previously published glioblastoma-targeted imaging studies. These results demonstrate that the fluorescent silica-coated nanoparticles can specifically target tumor-associated macrophages in the microenvironment surrounding primary tumors and they can be used as efficient nanoprobes for fluorescence imaging-guided surgery to improve glioblastoma outcome.

Year	Study	Characteristic
Kircher et al. 2003 [61]	Preclinical	Cross-linked iron oxide (CLIO) labeled with Cy5.5 is a metabolic targeting nanoparticle that is internalized and accumulated in tumor cells within a maximum of 24 h after injection.
Trehin et al. 2006 [49]	Preclinical	Cross-linked iron oxide (CLIO) labeled with Cy5.5 is a metabolic targeting nanoparticle that is internalized and accumulated in tumor cells within a maximum of 24 h after injection. Also seen in microglia and macrophages at the tumor border.
Cai et al. 2006 [62]	Preclinical	QDs coated with RGD peptides for targeting integrin of GBM. Significantly enhanced TNR (4.42) was achieved.
Jackson et al. 2007 [63]	Preclinical	High-dosed QDs coated with PEG phagocytized by tumor-induced inflammatory cells (macrophages and microglia) in the tumor border, but not by tumor or brain cells.
Orringer et al. 2009 [55]	Preclinical	The peptide F3, which targets the tumor cell surface receptor nucleolin, enhances uptake of the fluorescent polyacrylamide nanoparticles in glioma cells by a factor of 3.1.
Jiang et al. 2013 [64]	Preclinical	Molecular targeting with lactoferrin is also performed with a polymer-based nanoparticle.
Ni et al. 2014 [52]	Preclinical	Upconversion nanoparticles were labeled with angiopeptide-2 and PEG target GBM cells in mice.
Cui et al. 2015 [65]	Preclinical	Porphyrin-based nanostructure mimicking nature lipoproteins (PLP) for fluorescence-guided surgery. Accomplished tumor delineation at the cellular level and resulted in minimal residual tumor cells in the resection cavity.

Table 2.1 Overview of studies on nanoparticle-based agents for fluorescence-guided glioma surgery. (source from Ref. [46])

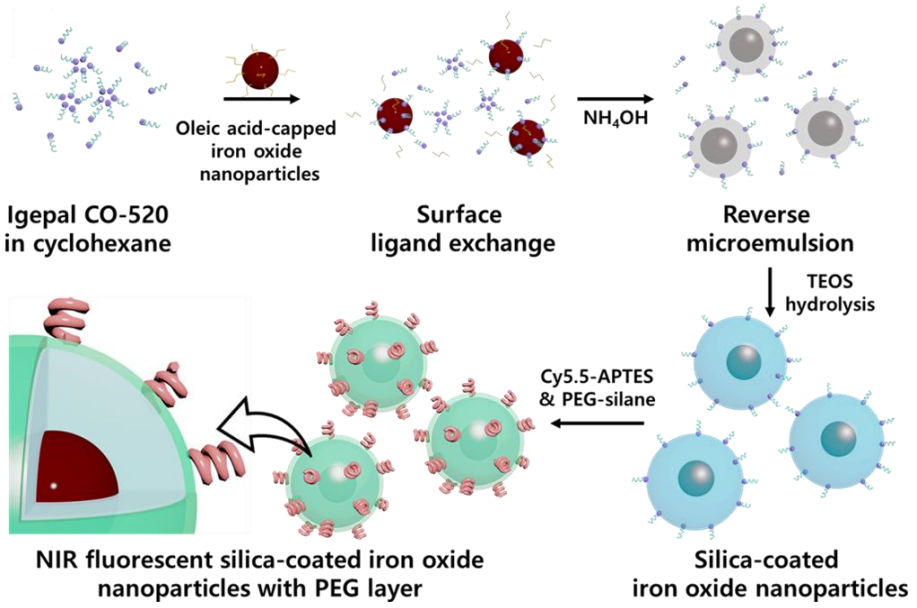

Figure 2.1 Synthetic illustration of NIR-fluorescent silica-coated iron oxide nanoparticles (NF-SIONs).

2.2. Experimental

Materials

3-(4,5-dimethylthiazol-2-yl)-2,5-diphenyltetrazolium bromide (MTT), 1,2-hexadecanediol, oleylamine (70%), benzyl ether, tetraethyl orthosilicate (TEOS), IGEPAL® CO-520, (3-Aminopropyl)triethoxysilane (APTES), dimethyl sulfoxide and phosphate buffered saline (PBS, tablet) were purchased from Sigma Aldrich. Ammonium hydroxide (28~30 wt.%), ethanol, methanol, acetone, n-hexane, cyclohexane, oleic acid, and diethyl ether was provided by Samchun chemicals (South Korea). SIH 6188.0 ([Hydroxy(polyethyleneoxy)propyl]triethoxysilane, 50% in ethanol) was provided by Gelest and iron(III) acetylacetonate was purchased from Strem Chemicals. Cyanine 5.5 dye (Flamma® 675 NHS ester) was from Bioacts (South Korea). All chemicals were used without any purification process.

Characterization

Transmission electron microscopy (TEM) images were obtained from LIBRA 120 (Carl Zeiss) at an accelerating voltage of 120 kV and the hydrodynamic size distribution measurement was conducted by using

DLS (Zetasizer Nano ZS, Malvern Instruments) equipped with a He-Ne laser operating at 633 nm and a back-scattering detector at 173°. Fluorescence excitation and emission spectra of NF-SIONs were studied through Photoluminescence spectroscopy (FluoroMate FS-2, Scinco). Inductively coupled plasma emission spectrometer (ICPS-7500, Shimadzu) was used to quantify the amount of iron of the NF-SIONs and their magnetization curve against the external magnetic field was obtained via PPMS-14 (Quantum design). In vivo and *ex vivo* fluorescence imaging of mouse model was achieved by using IVIS (Lumina XRMS; CLS136340, Perkin Elmer) and in vitro cell uptake and IHC assay was studied with a confocal microscope (A1 Rsi, Nikon).

Preparation of 8 nm-sized iron oxide nanocrystals

In order to acquire dual-functional imaging nanoprobes with MR and NIR fluorescent bimodality, magnetic iron oxide nanocrystals were reproduced by following previously reported method with minor modifications [66]. Typically, $Fe(acac)_3$ (350 mg), 1, 2-hexadecanediol (1.29 g), oleylamine (0.8 g), oleic acid (0.85 g) and benzyl ether (10 mL) were transferred into three-neck round bottom flask and magnetically stirred for 30 minutes. Residual moisture was removed by low-pressure

degassing at 100 ℃ for an hour. Then the mixture was heated to 300 ℃ (reflux) for an hour under Ar gas atmosphere. The resulted black solution was cooled down and acetone was added to precipitate the synthesized nanocrystals. The nanoparticles were collected at 8000 rcf centrifugation and the black sediment was recovered with n-hexane. The same precipitation and centrifugation procedure were repeated twice and finally, the nanoparticles were dispersed in cyclohexane (~5 $mg \cdot mL^{-1}$).

Synthesis of NIR-fluorescent silica-coated iron oxide nanoparticles (NF-SIONs)

A typical synthesis of silica coating process on iron oxide nanoparticles was referred to previous papers [58,67,68]. In 100 mL glass vial, cyclohexane (45 mL) and IGEPAL® CO-520 (2.3 g) were added and magnetically stirred for 5 minutes. Then, the prepared colloidal iron oxide solution (500 μL) and ammonium hydroxide solution (600 μL) were serially dropped into the solution by 5 minutes' intervals. It became blurred instantly but recovered to the transparent solution soon. After the addition of TEOS (150μL), it was kept for 10 hours with mild stirring. In situ PEGylation and NIR dye-labeling was achieved by injection of ready-made NIR dye-APTES complex and

commercial PEGsilane solution. In brief, flamma 675-NHS ester (10 μmol) and APTES (200μmol) were mixed in methanol (1 mL) to form Cy5.5-APTES complex and stirred during 24 hours in the fridge. After 10-hour silication process, the Cy5.5-APTES complex solution (100 μL) and SIH 6188.0 (400 μL) was serially added to the reaction mixture under mild stirring for 2 hours. The reaction was suddenly interrupted by acetone (30 mL) and soon, the aggregation of silica-coated nanoparticles was observed, and they were easily collected via centrifugation. The nanoparticles were fully redispersed in ethanol and precipitated with diethyl ether. Repeated twice, the collected nanoparticles were dialyzed in 0.01 M PBS solution for overnight to remove any residual solvents. Finally, the concentration of nanoparticles was set to 1 $mgFe \cdot mL^{-1}$ for further *in vitro* and *in vivo* experiments.

Photo-stability tests

Comparative study regarding the photo-stable characteristic of pristine dye and dye-loaded nanoparticles was conducted using a xenon arc light source (Lambda XL, Sutter instrument, USA). The distance between the light source and the cuvette was fixed. Then, the fluorescence intensity from two cuvettes with a dye-only solution and colloidal NF-SIONs

solution was measured at 675 nm wavelength by 1 minutes' interval under continuous illumination. The amount of Cy 5.5 in each solution was set to be identical, based on the calculated amount of loaded dye in NF-SIONs. The initial light intensity was measured by an optical power meter, then divided by the illuminated volume at the same position. The calculated power per unit volume was 2.65 $W \cdot cm^{-3}$ and hence the accumulated illumination dose was calculated as below.

Illumination dose $[J \cdot cm^{-3}]$

= Light power per volume $[W \cdot cm^{-3}]$ × Illumination time [s]

Dispersion stability tests

Dispersion stability of as-prepared nanoparticles was tested in cell media and PBS buffer solution with various concentration. The concentration of nanoparticles was set to 20 $\mu gFe \cdot mL^{-1}$ and each nanoparticle-containing solution was placed in a disposable cuvette. To prevent the evaporation, the cuvettes were capped with parafilm and kept in the dark area. By 30 days, DLS measurement was conducted after gentle shaking of cuvettes and each peak value was sorted in a graph.

MR phantom study

MR phantom images were taken using a 9.4 T/160 A animal MRI system (Agilent Technologies, Santa Clara, CA, USA) in T2 mapping mode. After the collection of T2 from each concentration, the linear relationship between the R2 (= 1/T2) and [Fe] was plotted. The transverse relaxation time was estimated by using MEMS (multi-echo multiple slices) sequences with a spin-echo readout. The detail sequence parameters were as follows: TR = 3000 ms, TE = 8.36 ms, NE = 16, average = 1, matrix = 128 × 128, FOV (Field of View) = 65.0 × 65.0 mm^2, slice thickness = 2.0 mm and scan time = 6.5 min.

Cell lines

Human malignant glioblastoma cell U87-MG and murine monocyte RAW 264.7 were distributed from Korean Cell Line Bank (Seoul, Korea) and grown in Dulbecco's Modified Eagle's Medium (DMEM, SH30243.01; GE Healthcare, USA) supplemented with 10% heat-activated fetal bovine serum (FBS, SH30919.03; GE Healthcare, USA) and 1% penicillin-streptomycin (15070-063; Life Technologies, USA). U87-MG cell line stably expressing firefly luciferase named U87-MG-luc was established as previously described for *in vivo* bioluminescence

imaging of glioblastoma orthotopic models. Human fibroblast CCD-986sk was obtained from the same distributor as other cell lines and maintained in Iscove's Modified Dulbecco's Medium (IMDM, SH30228.01; GE Healthcare, USA) with 10% FBS and 1% antibiotics. Cells were cultured at 37 ℃ in a humidified 5% CO_2 incubator.

Cellular toxicity assessments

The cellular toxicity of the as-prepared nanoparticles was investigated from RAW 264.7 and U87-MG cell lines. Each cell line was cultured in a 12-well plate (~1×10^5 cells per well) with a certain concentration of NF-SIONs. After incubating for 6, 12, 24 and 48 hours, the supernatant media was discarded and washed with 0.01 M PBS solution. Then, 1 mL of MTT (3-(4,5-dimethylthiazol-2-yl)-2,5-diphenyltetrazolium bromide, Sigma Aldrich) solution (0.5 $mg \cdot mL^{-1}$) was added to each well and the cells were incubated for an hour. Again, the supernatant solution was eliminated and 500 mL of DMSO was added to each well to break the cell membrane and dissolve the violet formazan crystals. Finally, the absorbance of each well was measured at 540 nm wavelength via microplate reader (mQuant, BioTek Instruments) and it was divided by that of the control experiment for relative comparison.

In vitro uptake tests

Cells were seeded in 10 mm-cover glass-bottom dishes at a density of 5×10^4, 24 hours before *in vitro* experiments. Nanoparticles were treated with serum-containing media to the cells by 10 μgFe·mL^{-1} at 37 °C for 4 hours. For cell nucleus and membrane staining, cells were soaked with phosphate buffered saline (PBS) gently so as not to be detached. Shortly afterward, cells were incubated with Hoechst (H3570, 1:500; Life Technologies, USA) in serum-free medium at 37 °C for 20 minutes and then with Wheat Germ Agglutinin (W11261, 5 μg·mL^{-1}; Life Technologies, USA) under the same condition as Hoechst staining for 10 minutes. Cells were visualized by a confocal microscope with ×20 magnification.

Mouse models

All animal experiments were carried out in accordance with the approved guidelines. All animal experimental protocols were approved by the Institutional Animal Care and Use Committee of Preclinical Research Institute in the Seoul National University Bundang Hospital (15099). 6-week-old male Balb/c nude mice were used in this preclinical

experiment and those mice were purchased from Doo Yeol Biotech (Seoul, Korea). The animals were anesthetized with 2% isoflurane gas and 1×10^7 U87-MG cells with cold PBS were injected into forelimb armpit of mice (n=3) subcutaneously with a sterile 26-gauge needle. After 2 weeks, U87-MG xenograft models were obtained for imaging experiment. To induce U87-MG glioblastoma orthotopic model, 5×10^4 U87-MG-luc cells with cold PBS were prepared. Mice were anesthetized with an intraperitoneal injection of zoletil (20 mg·kg-1) and xylazine (10 $mg \cdot kg^{-1}$). Then U87-MG-luc cells were injected into the brain striatum through an entry point 0.5 mm anterior and 2 mm lateral to the bregma with Hamilton syringe (n=3) [69]. Bioluminescence imaging (BLI) was conducted every three or four days for monitoring of tumor burden and growth on U87-MG glioblastoma orthotopic models. After 15 days, mice had substantial brain cancer at the point of imaging. All the animals had been administered on a regular diet and all experiments were performed in accordance with the guidelines by Institutional Animal Care and Use Committee (IACUC) and Seoul National University Animal Care.

Immunofluorescence staining

After euthanasia of glioblastoma orthotopic mouse models, brains were isolated and fixed by 4% paraformaldehyde in PBS, they were frozen with OCT compound at -80 ℃. Immunofluorescence staining method was utilized on 7 um-thick brain sections. All the slices were placed in 0.2% Tween 20 for 10 minutes and then incubated in 3% sodium deoxycholate solution on the shaker for 2-4 hours at room temperature. For blocking endogenous activity, 20-50% normal goat serum in 1% BSA-PBS solution was used and the slides were placed with this solution for 2 hours at 37 ℃. After that, staining of primary antibodies was conducted using GFAP (Ab5804, 1:200; Merck Millipore, Germany), CD11b (MCA711G, 1:200; Bio-Rad, USA), F4/80 (MF48000, 1:50; Life Technologies, USA), CD86 (553689, 1:80; BD Biosciences, USA) and Iba1 (Ab5076, 1:400; Abcam, UK), then slices were incubated overnight at 4 ℃. Finally, they were washed and incubated with Alexa fluor 488 (A11034, 1:400; Life Technologies, USA) for GFAP and Alexa fluor 594 (A11007/A11037/A11058, 1:400; Life Technologies, USA) for CD11b, F4/80, CD86 and Iba1, and Hoechst (H3570, 1:750; Life Technologies, USA) serially. Each stained section was mounted with Gel/Mount™ (Mø 1; Biømeda Corporation, USA).

The comparison of fluorescent images was observed with a confocal microscope.

In vivo fluorescence imaging

All animal experiments were carried out in accordance with the approved guidelines. All animal experimental protocols were approved by the Institutional Animal Care and Use Committee of Preclinical Research Institute in the Seoul National University Bundang Hospital (15099). Animals were anesthetized by 2% isoflurane gas and nanoparticles were administered intravenously with an insulin syringe. *In vivo* fluorescence images were acquired using *In vivo* Imaging System with the indicated wavelength (excitation: 660 nm, emission: 710 nm). Mice were kept alive and maintained body temperature at 37 °C during the imaging experiment. All images were analyzed by ImageJ software in terms of calculation of target-to-background (TBR).

2.3. Results and discussion

Synthesis and characterization of NIR-fluorescent silica-coated iron oxide nanoparticles (NF-SIONs)

Near-infrared fluorescent silica shell was coated onto 6 nm-sized iron oxide nanocrystals (**Figure 2.2**) according to the scheme shown in **Figure 2.1**. First, the ready-made oleic acid-capped monodisperse iron oxide nanoparticles were added to the solvent where the reverse microemulsions exist. Then the Igepal® CO 520, surfactant surrounded the iron oxide nanoparticles, exchanging the surface oleic acid [67]. When the ammonium hydroxide solution was added, the reverse microemulsions expanded and the surfactant coated iron oxide nanoparticles were incorporated into each droplet. After vigorously stirring for 5 minutes, tetraethyl orthosilicate was added and hydrolyzed to form primary silica layer. To achieve the highly sensitive fluorescence imaging through the *in vivo* imaging and immunofluorescence assay, Cy 5.5-labeled aminopropylsilane, and commercial PEG-silane were added to the reaction solution to import NIR fluorescence and dispersion stability. Molecular fluorophores often lose their fluorescence due to photon-induced chemical damages by external light sources, even during the microscopic studies. Thus, structural modification or encapsulation

process are commonly used to enhance their fluorescence stability [70]. As shown in **Figure 2.3A**, the overall morphology of synthesized NF-SIONs was observed through TEM analysis and their core/shell structure was clearly observed in the magnified image (inset). Their physical size was measured as 32.05±2.23 nm by calculating the average diameter of 100 nanoparticles from transmission electron microscopy images (**Figure 2.3B**) and mean hydrodynamic size in number distribution was about 37.84 nm by dynamic light scattering (DLS), meaning that the nanoparticles are well-distributed in the aqueous phase (**Figure 2.4A**). As can be seen from the fluorescence profile of NF-SIONs (**Figure 2.4B**), their excitation and emission spectra were close to that of pristine dye molecules (Flamma® 675 NHS ester, Ex. λ: 675 nm and Em. λ: 691 nm). Since the core iron oxide nanoparticles exhibit strong light absorption in visible wavelength area, it is highly important to control the distance of dye molecules from the iron oxide surfaces to reduce the excitation energy loss [71]. Thus, the iron oxide nanoparticles were coated with pure silica as a physical barrier. These core-shell nanoparticles were further coated with Cy 5.5 and PEG labeled silanes on their outer shell to form a second shell layer.

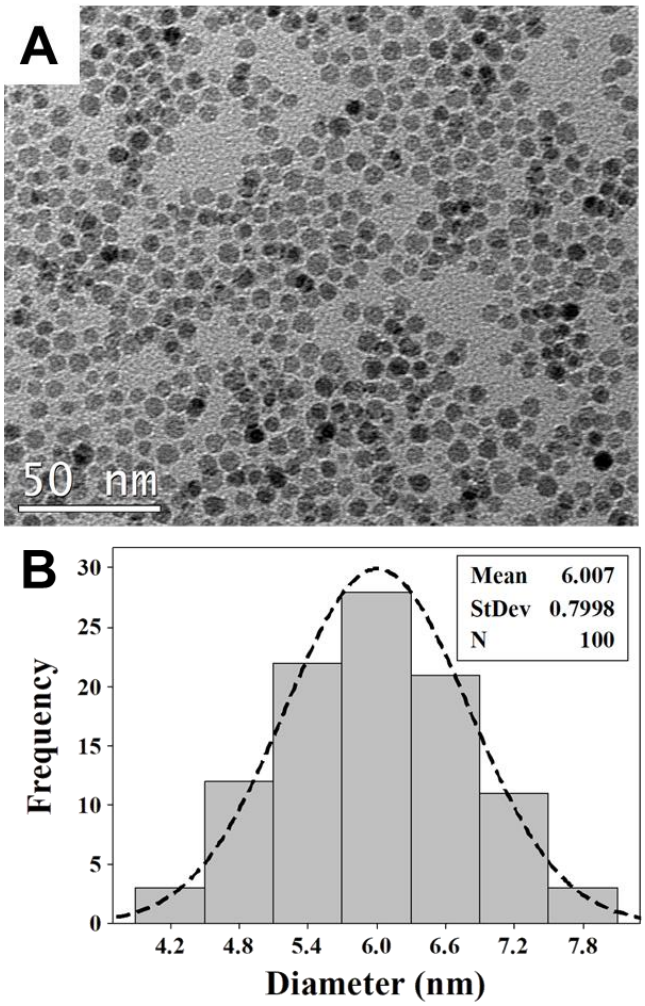

Figure 2.2 (A) Transmission electron micrograph image of core hydrophobic iron oxide nanoparticles and (B) a histogram plotted according to their physical size distribution.

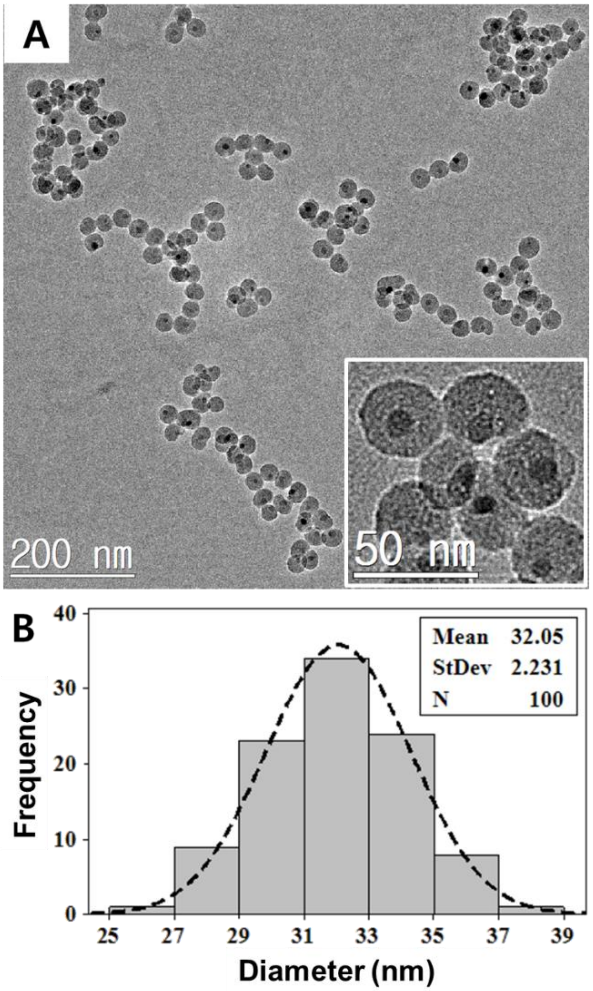

Figure 2.3 (A) Transmission electron micrograph image of synthesized NF-SIONs and (B) a histogram plotted according to their physical size distribution.

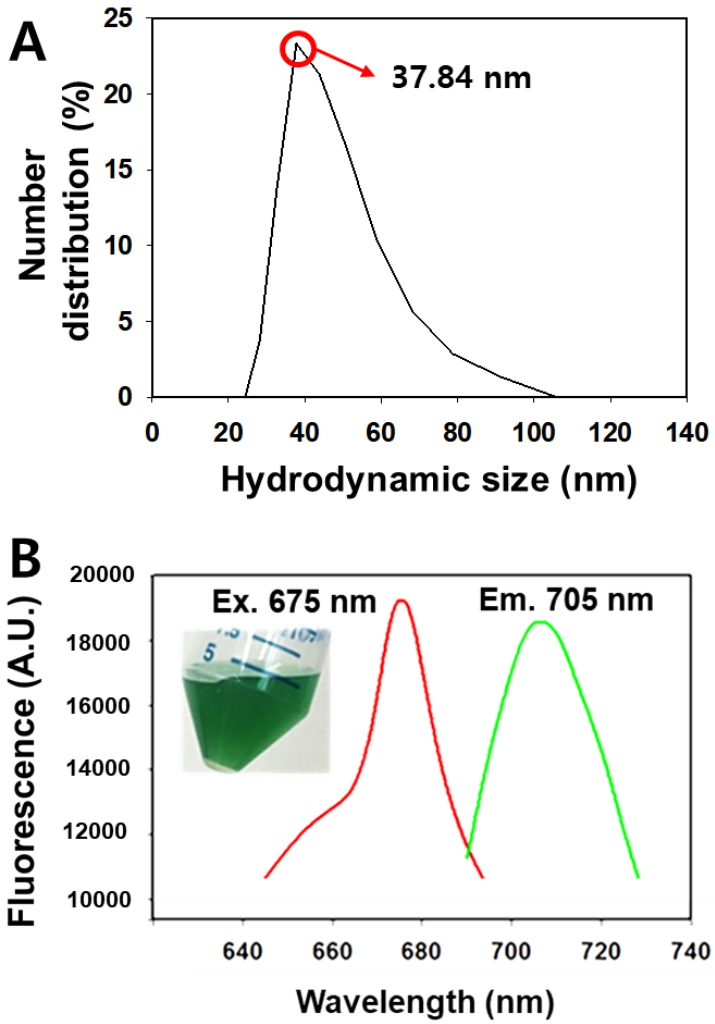

Figure 2.4 (A) Hydrodynamic size distribution of NF-SIONs in 0.01M PBS. (B) Excitation and emission profile of NF-SIONs.

Dispersion and fluorescence stability of NF-SIONs

One of the main obstacles of nanoparticles for bioimaging research is colloidal stability. Since the dispersion of nanoparticles is due to the surface charge in most cases, they are easily aggregated when introduced into buffer solution or body fluid-like media by the non-specific protein adsorption or charge neutralization by counterions. Hence, non-ionic PEG chains are usually used to prevent such irreversible aggregation and enhance colloidal stability through the circulatory system [72]. In this synthesis, the PEG chains were introduced onto the surface of NF-SIONs after the formation of the primary silica layer. To confirm their shelf life among the various conditions, PBS solution and DMEM media were equipped and set up as represented in **Figure 2.5A**. In each disposable cuvette, fresh DMEM media and concentrated PBS solutions (0.01 M to 0.1 M) containing nanoparticles (0.05 wt.%) were transferred and kept in dark, stable area for 2 months. The dispersion state was studied by DLS and the obtained results were summarized in **Figure 2.5B**. For the first 30 days, there was no significant change either from the camera shot or from the DLS number distribution. After 60 days, however, the nanoparticles showed severe aggregation at the 0.1 M PBS and DMEM media.

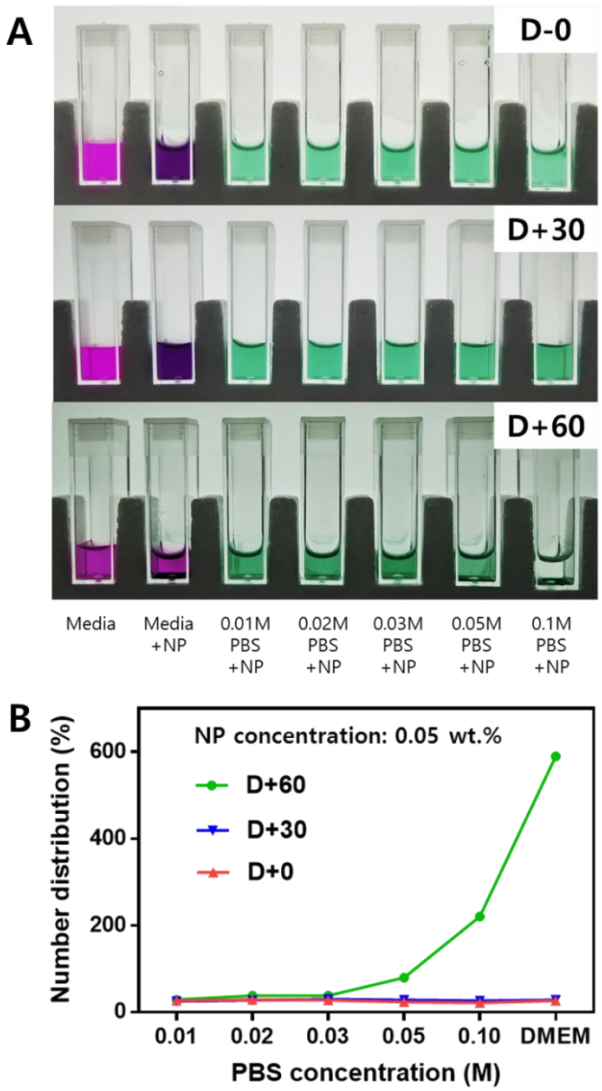

Figure 2.5 (A) Dispersion stability test (~60 days) among cell culture media and PBS with various concentration. (B) Hydrodynamic size change observation through DLS measurement. The concentration of nanoparticles was 0.05 wt.%

Fluorescence stability of NF-SIONs was also investigated by comparing the fluorescence decaying patterns of Cy 5.5 dye solution and colloidal NF-SIONs. Each diluted solution was irradiated for a minute with xenon light source and the fluorescence intensity was measured. The experiment was repeated for 6 times and the obtained fluorescence intensity as a function of exposure time was plotted as **Figure 2.6A** after normalization. Using the measured light energy density, the illumination doses depend on the irradiation time in X-axis were calculated. Apparently, the severe fluorescence decay (over 60%) was observed from the free-standing Cy 5.5 solution, while there was no remarkable change (less than 10%) occurred in the case of the colloidal NF-SIONs, meaning that the NF-SIONs have superior fluorescence stability compared to free-standing dyes. Furthermore, the amount of fluorescent dye contained in 1mg of NF-SIONs was measured using standard fluorescence curves of Cy5.5 and NF-SIONs, and it was found to be about 6.3 nmol (**Figure 2.7**).

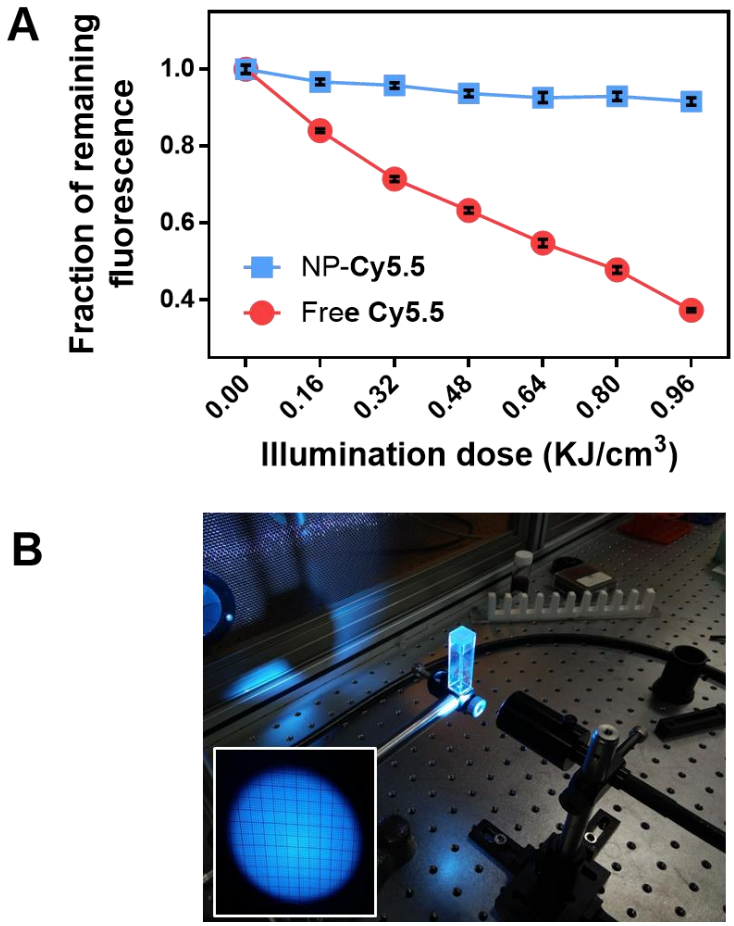

Figure 2.6 (A) Photobleaching comparison of Cy 5.5 dye and NF-SIONs in DI water under xenon light irradiation for 6 minutes. The concentration of nanoparticles was 0.05 wt.%. (B) Photo of xenon lamp radiation set up using transparent disposable cuvette. Light power per area was measured by grid paper (inset).

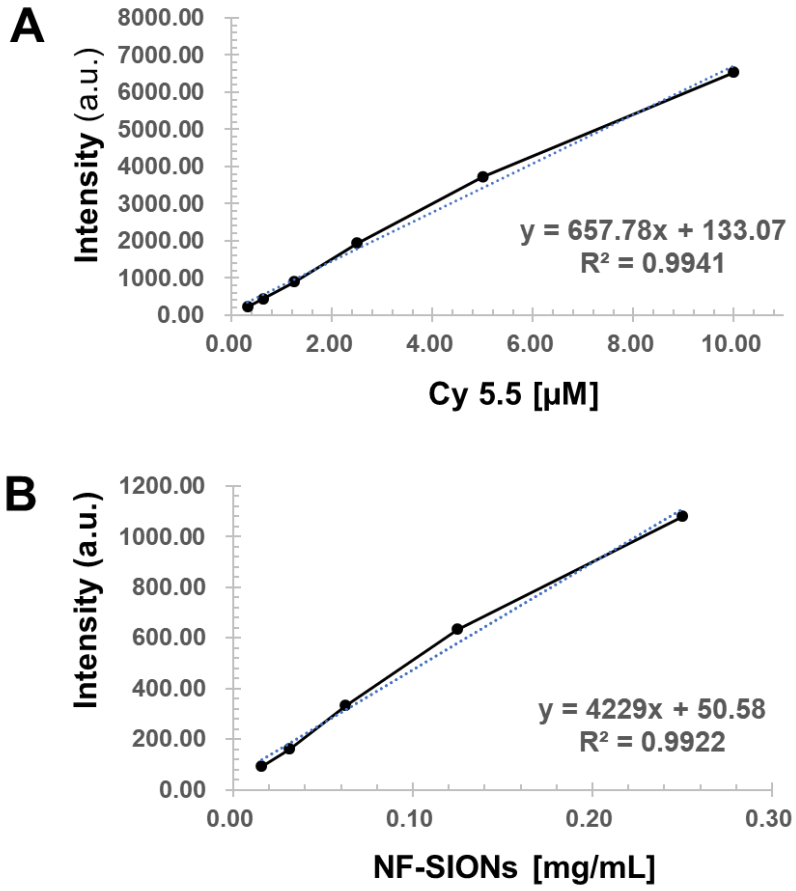

Figure 2.7 Standard curves of fluorescence intensity from (A) Cy 5.5 stock solutions and (B) NF-SIONs colloidal solutions.

The magnetization of NF-SIONs and MR phantom imaging

The magnetic property of NF-SIONs was analyzed by drawing the magnetic hysteresis (M-H) curve in an applied field ranging from -10 ~ 10 kOe at 293 K (**Figure 2.8A**). The M-H curve showed no remnant magnetization after the applied magnetic field was removed, which means that the NF-SIONs are superparamagnetic, and saturation magnetization (Ms) was calculated as 3.80 $emu \cdot g^{-1}$. Such low Ms value is attributed to the diamagnetic contribution of the silica shell, which occupies a large portion of core-shell nanoparticles [73]. To investigate the MR imaging performance of NF-SIONs, the phantom test was conducted following the previously reported method [74]. As plotted in **Figure 2.8B**, serially diluted NF-SIONs showed linear regression in R2 relaxation, and the r_2 (specific relaxivity) was calculated as 95.86 $mM^{-1}s^{-1}$, which is similar or a little less than that of commercialized iron oxide-based contrast agents [75]. These results suggest that our NF-SIONs might be properly used in MR imaging applications.

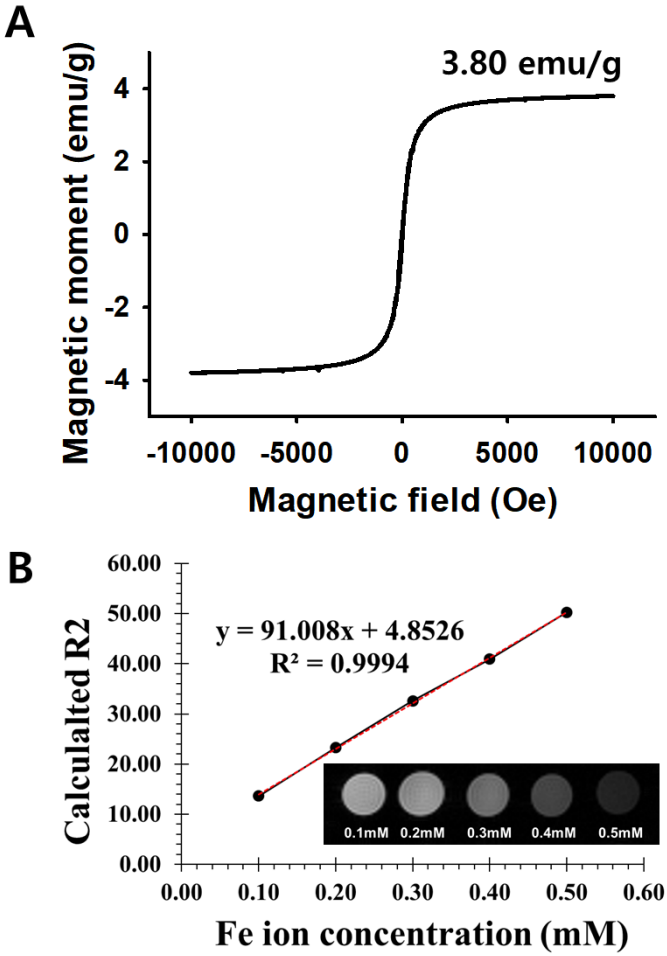

Figure 2.8 (A) SQUID magnetization measurement of the NF-SIONs powder. (B) R2 relaxation rates as a function of iron concentration (mM) of NF-SIONs dispersed in DI water, measured at 25 °C and 9.4 T. Inset image represents T2-weighted MR enhancement of NF-SIONs in various concentration.

Cytotoxicity test of NF-SIONs

The cytotoxicity of silica particles and silica-coated iron oxide nanoparticles have been extensively studied in former researches [76,77]. Here, the cytotoxicity of the as-prepared NF-SIONs was assessed from two cell lines (U87-MG; human brain tumor, RAW 264.7; mouse macrophage) prior to *in vivo* bioimaging. As shown in **Figure 2.9**, the viability against the nanoparticles was tested via MTT assay. Overall, the relative viabilities from the two cell lines used in the experiment were inversely proportional to the concentration of nanoparticles and the treatment time. However, more than 90% of the cells survived even at a high concentration (200 $\mu gFe \cdot mL^{-1}$) and long incubation time (48 hours), proving that the as-prepared NF-SIONs are biologically safe for further experiments.

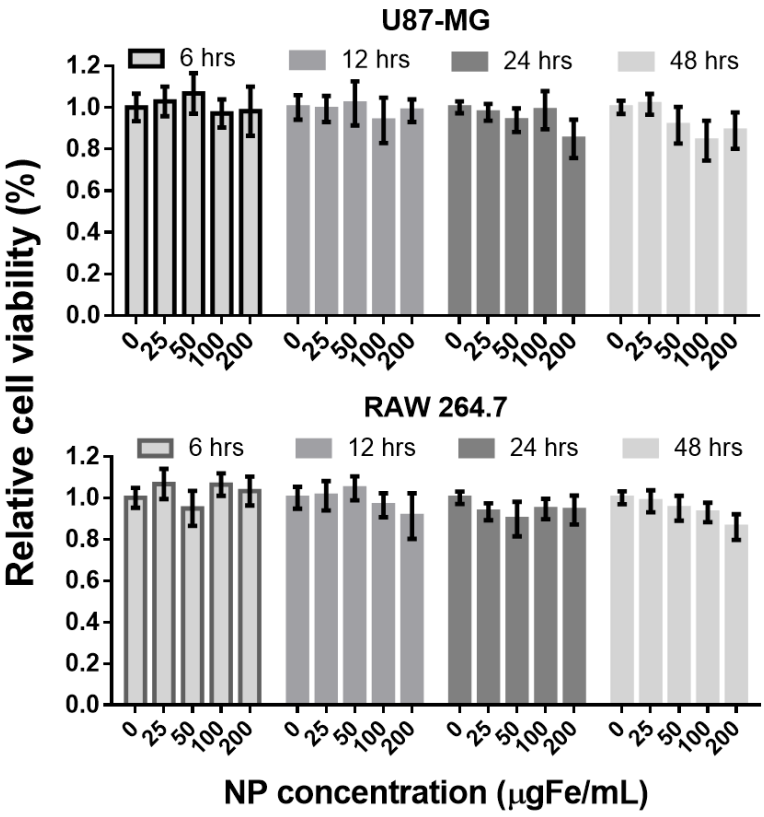

Figure 2.9 MTT assay results of NF-SIONs against U87-MG and RAW 264.7 cell lines.

NF-SIONs preferentially stains glioblastoma cells and TAMs *in vitro*

Having shown that the adverse effects of the NF-SIONs on cell viability were minimal, the preferential cellular uptake of NF-SIONs was studied using different cell lines; glioblastoma cells (U87-MG) and tumor-associated macrophages (TAMs, RAW 264.7) as therapeutic targets and normal parenchyma cells (CCD-986sk) as control. Confocal microscopy revealed an apparent preference of NF-SIONs for U87-MG glioblastoma cells and RAW 264.7 macrophages over CCD-986sk fibroblasts after 4-hour incubation with 10 $\mu gFe \cdot mL^{-1}$ of NF-SIONs as shown in **Figure 2.10**. NF-SIONs proved to be robust for probing glioblastoma cells and TAMs selectively *in vitro*, which implies theirs *in vivo* targeting potential to delineate glioblastoma.

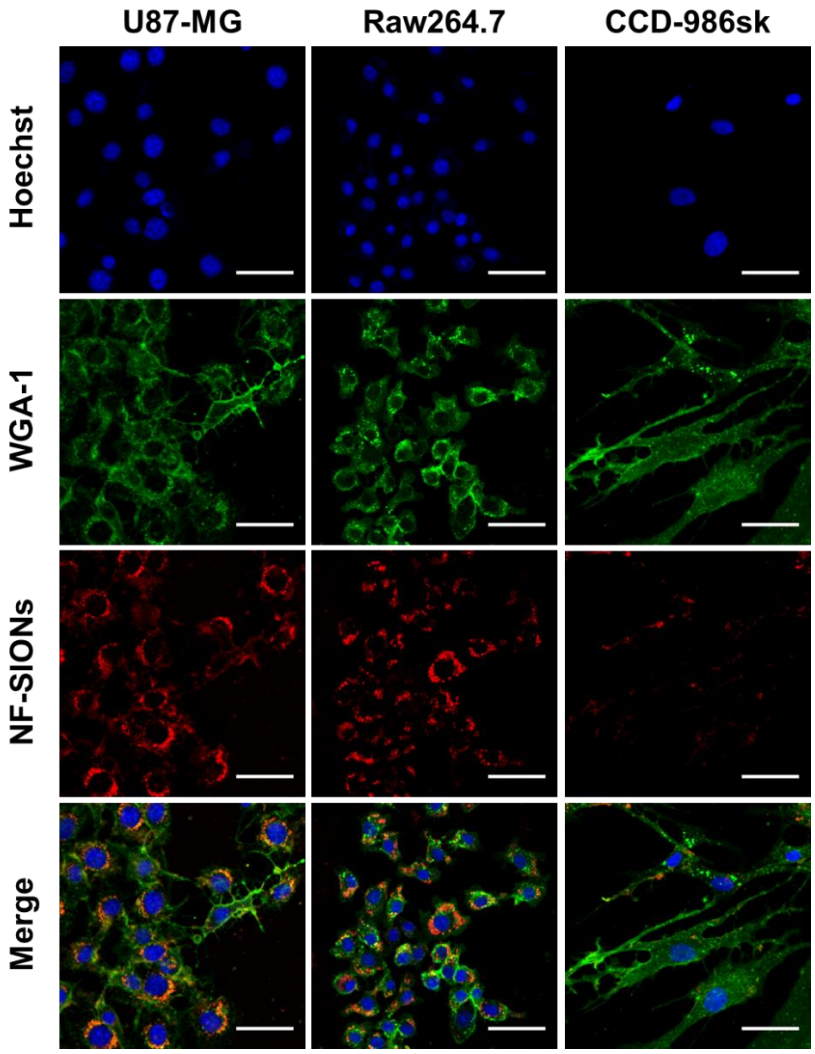

Figure 2.10 In vitro cellular uptake study of U87-MG, RAW 264.7 and CCD-986sk cell lines. Shown are confocal micrographs of cell lines that cultured for 4 hours with NF-SIONs containing medium (10 μgFe·mL^{-1}). Scale bars: 50 μm.

NF-SIONs show high uptake for glioblastoma and rapid background clearance through urination in subcutaneous xenograft model by *in vivo* fluorescence imaging

It is well-known that subcutaneously injected nanoparticles accumulate passively near tumor regions by enhanced permeability and retention (EPR) effects, due to the architectural abnormality of neovascularization and low association with the adjacent lymphatic system [78,79]. Since extremely small nanoparticles (<~10 nm) can be rapidly removed (excreted) by urination and larger particles (>~200 nm) can be removed by the mononuclear phagocyte system (MPS), nanoparticles with intermediate size (10~200 nm) with neutral surface charge and biocompatible coating are highly preferred as suitable bioimaging nanoprobes for efficient vascular delivery [80,81]. Therefore, in this study, NF-SIONs were designed to be in the range of 30-50 nm with a non-ionic surface so that the nanoparticles can not only be transmitted to the whole body including the tumor but also safely excreted via the urinary system. As shown in **Figure 2.11**, the synthesized NF-SIONs (200 μgFe) were injected into the tail vein of glioblastoma-bearing mice and systemic fluorescence imaging was performed for up to 24 hours. Although it showed significant uptake of

nanoparticles not only by tumor but also by liver and intestine up to 8 hours, 24 hour-post images indicated that our nanoprobe successfully delineated glioblastoma tumor (the right shoulder region) with high specificity after thorough clearance from the blood and other organs. Also, as seen in the inset images, the fluorescent signals in the bladder and external genitalia indicated that non-targeted NF-SIONs were well-excreted in the urine.

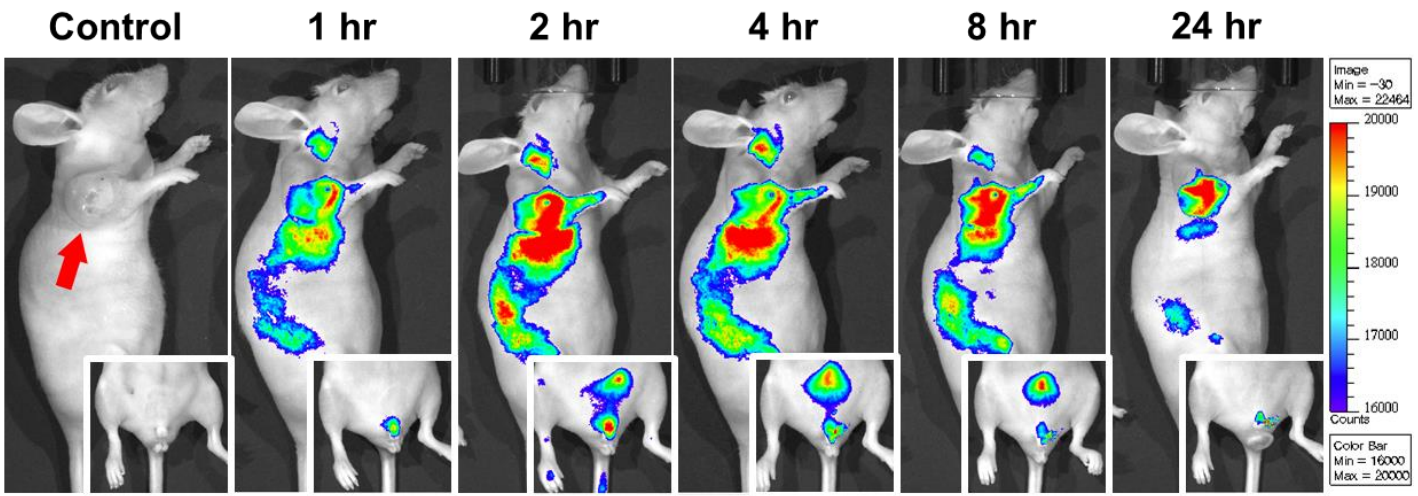

Figure 2.11 Non-invasive fluorescence imaging of NF-SIONs in the glioblastoma xenograft models for 24 hours to study biodistribution of administered nanoparticles. The inset images show the traces of nanoparticles excreted through the external genitalia.

To analyze the observed fluorescence signals around the tumor with cellular resolution, the tumor and adjacent tissue were excised (24 hours after nanoparticle injection) and immunofluorescence study was performed using confocal microscopy. Based on the results in **Figure 2.10**, the tumoral distribution of nanoparticles was analyzed using several cellular markers such as Ki-67 (proliferating tumor cells), CD31 (endothelial cells/macrophages), F4/80 (tumor-associated macrophages), and CD11b (monocytes/macrophages) as shown in **Figure 2.12**. Interestingly, most of the nanoparticles-binding cells expressed macrophage-related F4/80 and CD11b. The nanoparticle signal, however, did not colocalize with Ki-67 positive tumor cells and CD31 positive endothelial cells surrounding the lumen of a blood vessel (an arrow). This is contrary to the fact that the cellular uptake study is shown in **Figure 2.10**, which did not reveal a large difference in nanoparticle internalization between tumor cells and macrophage cell lines. This may have induced due to differential uptake ability of general macrophages and tumor-associated macrophages which were activated by secretion of chemokines from the tumor. Although cellular targeting ability of the developed nanoprobe did not show the prominent difference between tumor cells and macrophages under *in vitro* condition, their *in vivo*

specificity for activated tumor-associated macrophages over glioblastoma cells was successfully confirmed by immunohistology analysis. Therefore, it was concluded that the nanoparticles injected into the body were well accumulated around the tumor due to the EPR effect through neovasculature, but they were mostly taken up by tumor-associated macrophages, activated and endocytosis enhanced macrophages due to several chemokines secreted from the tumor, rather than by the tumor cells.

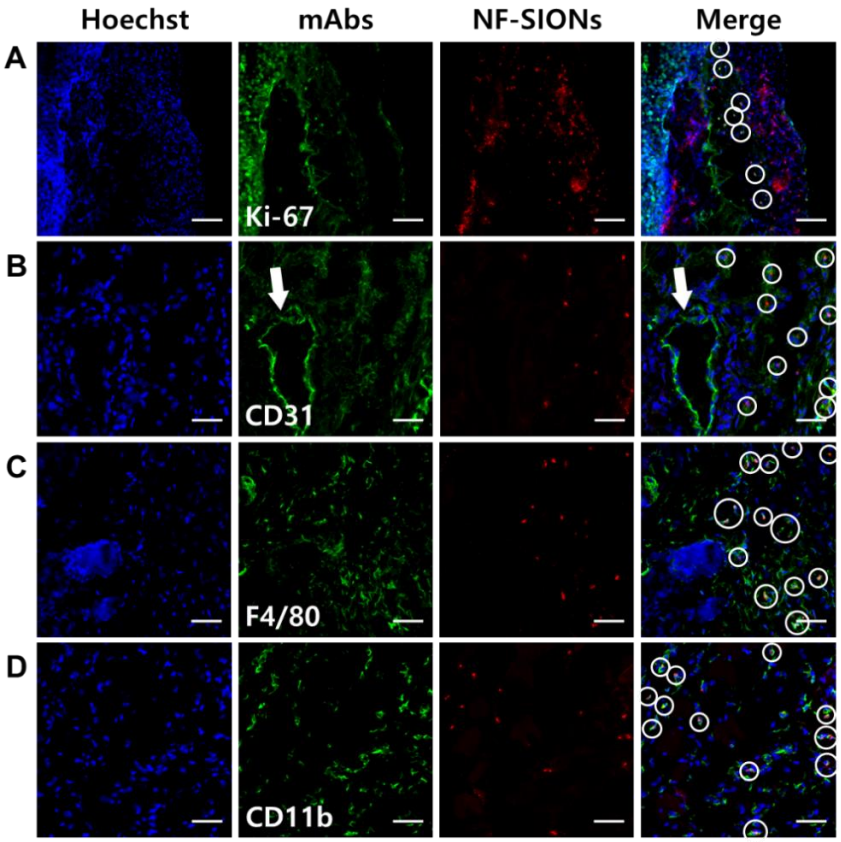

Figure 2.12 Characterization of targeting and distribution of NF-SIONs in the shoulder tumor region by immunofluorescence staining, 24 hr after injection. The shown sections were stained with monoclonal antibodies (mAbs; green) against Ki-67 (A, proliferating cells), CD31 (B, endothelial cells), F4/80 (C, murine macrophages), and CD11b (D, monocytes/macrophages). White circles indicate co-localization of TAMs and NF-SIONs. Arrow; lumen of the blood vessel. Scale bar: 100 μm (×20) for A and 50 μm (×40) for B, C, and D.

NF-SIONs penetrate the blood-brain barrier and delineate glioblastoma specifically in orthotopic xenograft model by *in vivo* fluorescence imaging.

Considering the primary nature of the U87-MG cell line, in-depth comparisons were performed to confirm the specific uptake of nanoparticles in the orthotopic model as well as in the subcutaneous model. Unlike elsewhere, the central nervous system is protected by a robust defense system called the blood-brain barrier (BBB), which is a major obstacle to the development of drugs and nanoparticles for brain-related diseases [82]. However, recent studies of the relationship between glioma and BBB have shown that tumor cells can disrupt the BBB system and damage the tight junctions, allowing hydrophilic nanoparticles to enter [83–86]. Therefore, it was expected that NF-SIONs with high dispersion stability and hydrophilicity will flow into the brain through the damaged BBB despite its relatively large size. As in the imaging study with subcutaneous xenograft models, NF-SIONs were injected through the tail vein, and the fluorescence signals in the whole body and each organ were analyzed up to 24 hours at regular intervals, as shown in **Figure 2.13**. Intracranial glioblastoma uptake of NF-SIONs showed the peak signal in 24 hours after injection. Non-

targeted NF-SIONs were smoothly excreted through the kidneys and the bladder (urine) confirmed by *ex vivo* fluorescence signal analysis (TBR data in **Figure 2.14**). Although abdominal organ uptake is still high at 24 hour-post injections, 24 hour-post injection images showed an obvious contrast between glioblastoma region and normal brain parenchyma, providing a decent tool for intraoperative guidance of glioblastoma resection.

Figure 2.13 Biodistribution study of NF-SIONs in the orthotopic tumor models among 24 hours by non-invasive fluorescence imaging.

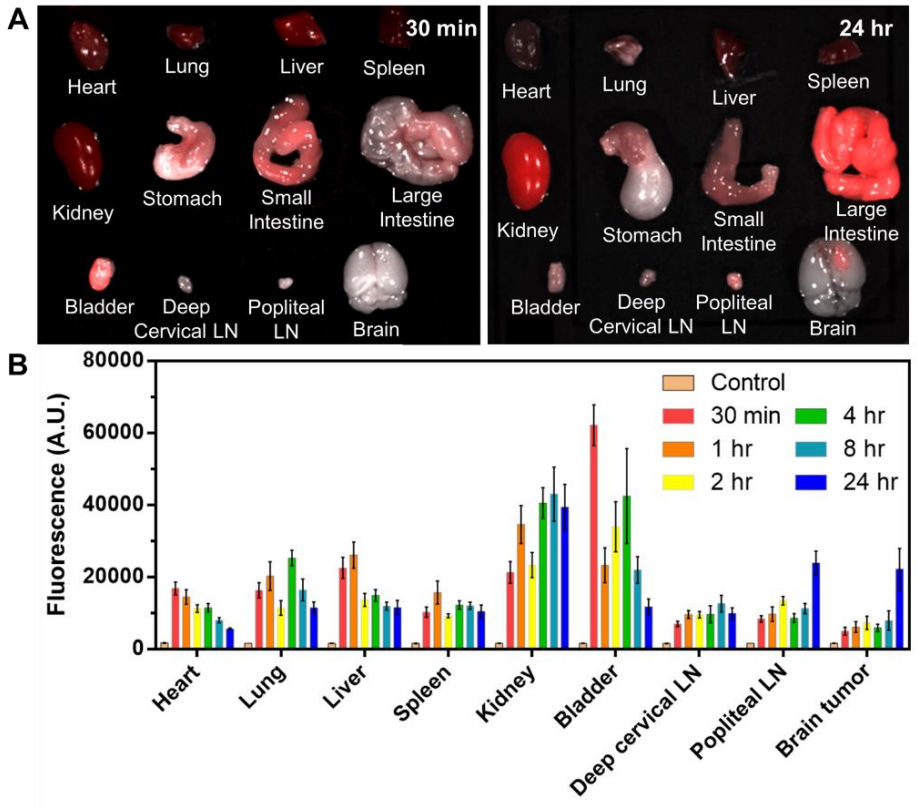

Figure 2.14 (A) Fluorescence images of resected organs at 30 mins and 24 hours after injection of NF-SIONs. (B) Target-to-background ratio (TBR) comparison of fluorescence intensity for each organ by the time taken after injection (FOV: 7.5).

Having shown the ability to specifically targets glioblastoma via *in vivo* whole body and *ex vivo* organ imaging, immunofluorescence staining of the excised brain from the orthotopic model (8 hours after injection) was also demonstrated to identify the characteristics of the NF-SIONs' cellular localization. The *ex vivo* fluorescence signal was observed to be strongest in the brain 24 hours after injection, but at the tissue level fluorescence analysis, the brain sample at 8 hours after injection showed better results. The distribution of NF-SIONs in the right and the left sides of the brain was compared corresponding to the tumor and the non-tumor regions, respectively, to verify *in vivo* and *ex vivo* imaging data. Indeed, most NF-SIONs binding cells were localized in the tumor region (**Figure 2.15** and **2.16**) showing specific targeting of glioblastoma area whereas almost no NF-SIONs positive cells were found in the normal brain region. Specifically, most of the NF-SIONs bound to macrophages ($CD31^+$ or $F4/80^+$ or $CD11b^+$) or microglia ($Iba1^+$, brain macrophages), but not astrocytes (GFAP) as shown in **Figure 2.15** and **2.16**. Some of the Ki-67^+ cells, indicative of proliferating cancer cells, were overlapped with the NF-$SIONs^+$ cells as presented in **Figure 2.15A**, however, further examination is required because they might be proliferating inflammatory cells (Ki-67^+ and $CD11b^+$ cells) as confirmed

by dual staining with CD11b monocytes/macrophages marker in **Figure 2.16B**. Overall immunofluorescence analysis showed that the injected NF-SIONs were selectively caught by tumoral region compared to the non-tumor region, and they were specifically taken up by the tumor-associated immune cells (monocytes/macrophages/microglia) over brain parenchyma cells (astrocytes).

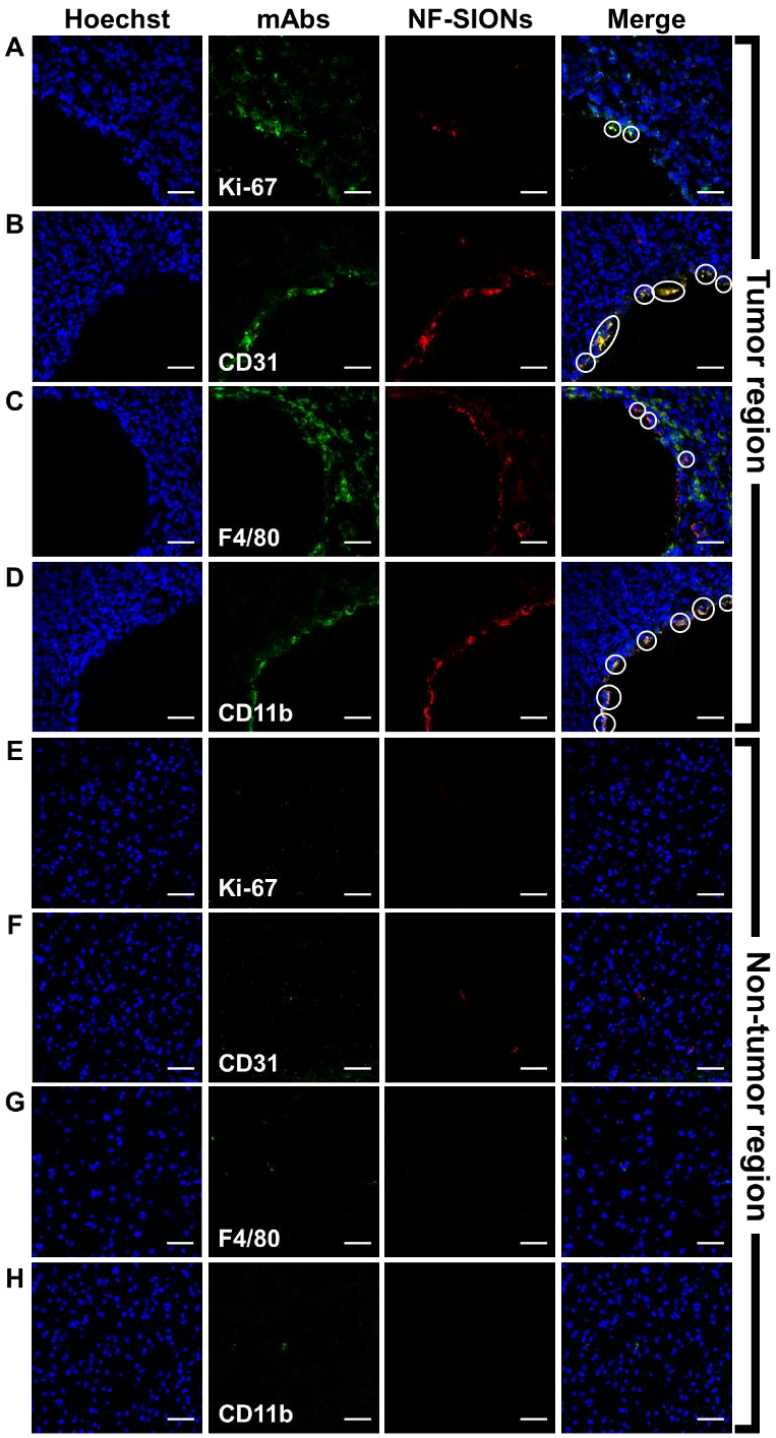
Hoechst
mAbs
NF-SIONs
Merge
A
Ki-67
B
CD31
C
F4/80
D
CD11b
E
Ki-67
F
CD31
G
F4/80
H
CD11b
Tumor region
Non-tumor region

Figure 2.15 Characterization of targeting and distribution of NF-SIONs in the brain tumor region (A-D) and non-tumor region (E-H) by immunofluorescence staining, 8 hr after injection. The shown sections were stained with monoclonal antibodies (mAbs; green) against Ki-67 (A and E, proliferating cells), CD31 (B and F, endothelial cells/macrophages), F4/80 (C and G, macrophages), and CD11b (D and H, monocytes/macrophages). White circles indicate co-localization of TAMs and NF-SIONs, and the hole seen in the tumor region was due to the injection process of tumor cells. Scale bar: 50 μm (×40).

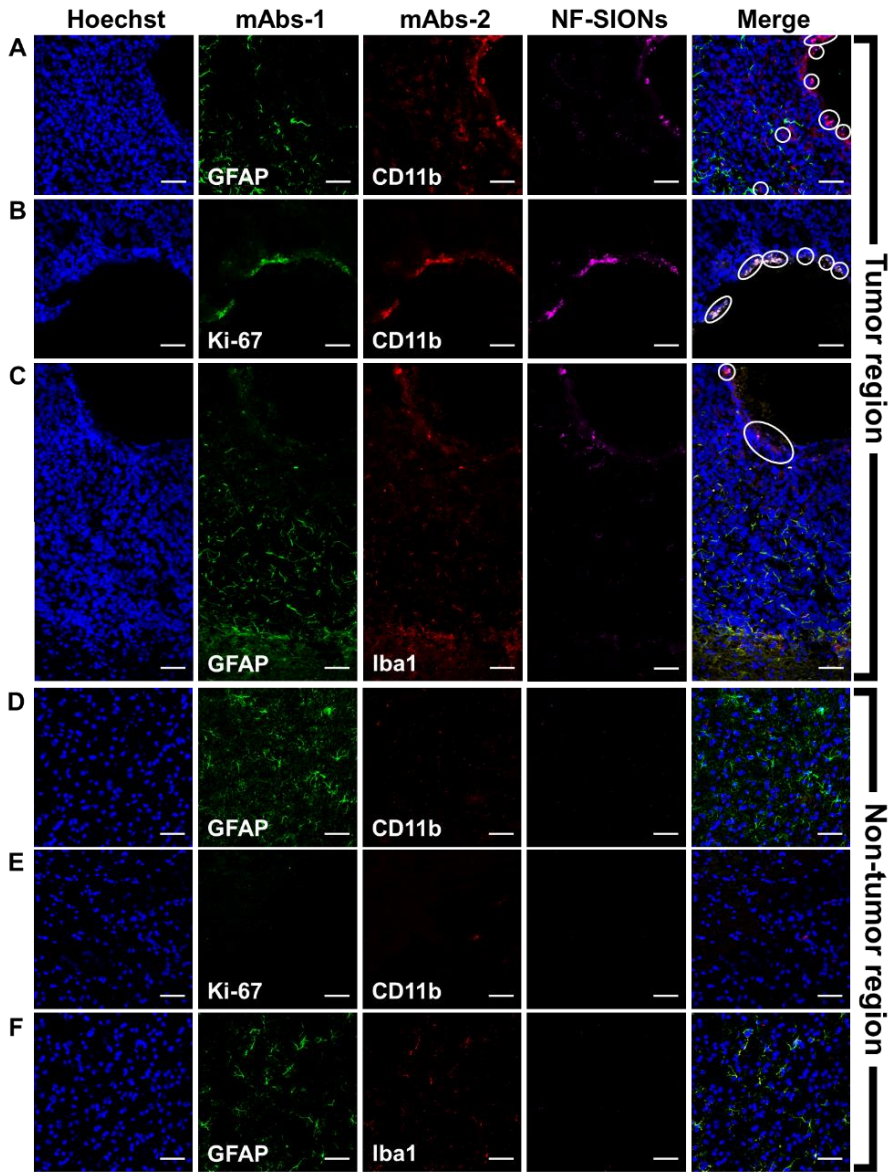

Figure 2.16 Characterization of targeting and distribution of NF-SIONs in the brain tumor region (A-C) and non-tumor region (D-F) by immunofluorescence staining, 8 hr after injection. The shown sections

were stained each with two monoclonal antibodies (mAbs; green and red) against GFAP (A, C, D, and F, astrocyte), CD11b (A, B, D and E, monocytes/macrophages), and Iba1(C and F, microglia). Compared with the non-tumoral region, macrophages and microglial cells were highly expressed in the tumor region, and nanoparticles-binding cells were well overlapped with tumor-associated macrophages/microglias ($CD11b^+$ or $Iba1^+$ cells), but not with astrocytes ($GFAP^+$ cells). White circles indicate co-localization of TAMs and NF-SIONs, and the hole seen in the tumor region was due to the injection process of tumor cells. Scale bar: 50 μm (×40).

2.4. Summary

In this study, facile synthesis of dual-modal imaging nanoparticles with improved dispersibility and robust fluorescence properties was introduced and their application as tumor-associated macrophage-specific probes for fluorescence-guided surgery of glioblastoma in murine xenograft models was demonstrated. After confirmation, the suitability of the NF-SIONs for *in vivo* experiments via MTT assay and cell uptake test, *in vivo* fluorescence imaging was performed in subcutaneous and orthotopic xenograft models to analyze time-course *in vivo* behaviors of nanoparticles and their uptake pattern by the immune cells in the tumor tissues. By performing *in vivo* fluorescence analysis for 24 hours, it was shown that the administered nanoparticles were well excreted in the urine and remained only in the tumoral region. In addition, immunofluorescence staining using various monoclonal antibodies showed that the injected nanoparticles exhibited a high uptake in tumor-associated immune cells (monocytes/macrophages/microglia) over cancer cells and brain parenchymal cells. Overall, the NF-SIONs were proposed as a valuable tool to improve the outcome of the glioblastoma surgery by providing additional information on tumor-associated macrophages.

Glioblastoma is a deadly cancer due to its invasive and infiltrative features. For complete surgical resection of glioblastoma, which is the most effective therapeutic option, an *in vivo* fluorescence imaging technique was developed using highly water dispersible and fluorescently stable NF-SIONs and their feasibility to guide the distribution of tumor-associated macrophages was successfully demonstrated. Although the nanomaterial-based approach to imaging macrophages given their naturally high endocytosis activity is well-known, there have been few trials to use this technique to surgically visualize tumor microenvironment focusing on specific localization of tumor-associated macrophage in the glioblastoma and their significant role for tumor prognosis. Clinical trials of molecular imaging technique using nanoparticles are now vibrant such as C dots based optical-PET imaging [87]. Future study to show the potential of our developed nanoprobe for MRI based glioblastoma diagnosis will booster clinical translation of tumor-associated macrophage targeting NF-SIONs imaging to provide a one-shot serial imaging strategy from preoperative diagnosis to intraoperative guidance. This will make the clinical management of glioblastoma more effective.

Chapter 3.

Translocator Protein 18 kDa-Targeted Near-Infrared Fluorescent Ultra-Small Iron Oxide Nanocrystal for Glioblastoma Imaging

3.1. Introduction

Among the intracellular targets, the translocator protein 18 kDa (TSPO) is one of the most investigated and promising, as it appears to be over-expressed in some types of cancers, including breast, colon, prostate, ovarian and brain (such as glioblastoma) compared to healthy tissues. In particular, TSPO is located in the outer membrane of mitochondria as a component of a multi-proteic complex named mitochondrial permeability transition pore (MPTP), involved in various cellular functions including cholesterol transport, steroid hormone synthesis, mitochondrial respiration, permeability transition pore opening, programmed cell death (apoptosis) and proliferation [88–92]. TSPO has, therefore, become an attractive subcellular target for both the early detection of disease states involving its overexpression and the selective mitochondrial drug delivery [93]. The amount of structurally different TSPO ligands examined has increased over time revealing a broad spectrum of actions, such as anti-steroidogenic or pro-apoptotic effects potentially useful for cancers therapy [88]. In recent times new PET imaging probes and various metal-based complexes targeting the TSPO have been projected to monitor the TSPO expression in neuropathological diseases such as neuroinflammation and tumors [94–

99]. Specifically, Glioblastoma multiforme (GBM) is the most common and deadly type of primary brain cancer. Although GBM patients have currently available therapies, including radiation and chemotherapy with temozolomide, the median survival is less than 14 months after diagnosis mainly due to the occurrence of resistance phenomena. Complete surgical resection of GBM is critical to improving GBM treatment. Therefore, the discovery of new targets for early diagnosis and GBM therapy is becoming increasingly necessary [100]. For an advanced diagnosis of tumors, the essentials characteristics of the imaging probes are a high affinity for the target sites, selective cellular internalization, and an *in vivo* high stability. In addition, such probes are required to be non-toxic and easy to prepare. Since TSPO is selectively overexpressed in the brains of the GBM patients [100], TSPO ligands can be exploited as targeting moiety for the early diagnosis and successful delineation of GBM by means of *in vivo* fluorescence and nuclear imaging, as well as for the glioblastoma therapy. In addition to the identification of new targets for GBM, a winning strategy could be the use of appropriately engineered nanoparticles systems able to selectively target the glioblastoma cells. This would overcome the limits of the classical molecules currently used for the diagnosis and therapy of brain cancers,

including the difficulty of crossing the blood-brain barrier (BBB). Moreover, approaches to increase the delivery of pharmacologically active molecules to the brain tissue without opening of the brain vascular system are urgently needed and for this purpose, nanoparticles represent an effective opportunity to reach this target, especially in cerebral tumors. Ultra-small superparamagnetic iron oxide nanoparticles (USPIONs) are particularly promising since their magnetic properties increase the number of potential applications in the biomedical area, including drug delivery, thermotherapy, imaging and detection of the tumor. Their potential to cross biological barriers, including the BBB and the blood-brain tumor barrier (BBTB), has been recently confirmed by Kenzaoui et al. [101–103] using an *in vitro* model representative of the endothelial-glioblastoma tumor barrier. They demonstrated that USPIONs can be translocated from endothelial cells to glioblastoma cells. The selection of the surface molecules for iron oxide nanoparticles is crucial for biological uses, since the good stability in the physiological buffer, the biocompatibility, and the prevention of the nonspecific interaction with a cell, are strictly dependent from this issue. In particular, low molecular weight polyethylene glycol (PEG) has been paid a lot of attention as a potential organic surface molecule from a biomedical point of view. PEG

anchored on the surface of NPs leads to decrease nonspecific binding with cells and enhances viability and stability by retaining a helical conformation of the crystalline state in water [104]. For these reasons, PEGylated USPIONs were chosen to be used following the one-step synthesis method previously reported [105]. In particular, it was designed to graft a lab-made imidazopyridine based TSPO ligand on the surface of iron oxide nanoparticles, as a targeting moiety [106,107], and conjugate near-infrared (NIR) emitting fluorescent dyes in order to perform *in vivo* fluorescence imaging for diagnosis and successful delineation of GBM. The use of targeted nanoplatform-based probes aims to extend plasma half-lives, thus increasing *in vivo* stability and targeting efficiency. Several TSPO-targeted nanoparticles have been yet proposed as potential and efficacious fluorescent agents for visualization of trafficking inside the cell and for *in vivo* imaging [106,108,109]. Optical imaging consents several advantages, including accurate sensitivity, non-invasive procedure, and a reasonable cost of the instrument for the detection. Remarkably, the use of fluorescent probes emitting in the near-infrared region (NIR, 700-1100 nm), can enhance the signal-to-noise ratio through *in vivo* technique of optical imaging. In the NIR region, autofluorescence and scattering by biological tissues are

minimal, therefore NIR probes are expected to result in high resolution and deep penetration images [110].

The novel synthesis TSPO-targeted-NIR-fluorescent ultra-small iron oxide nanoparticles have been thoroughly investigated, assessing the NIR emitting properties upon surface functionalization with TSPO ligand, and elucidating the morphology, size, colloidal stability of the nano-objects in each step of preparation. Various techniques have been applied for the characterization of this system, such as transmission electron microscopy (TEM), dynamic light scattering (DLS) and fluorescence spectroscopy. *In vitro* toxicity study of TSPO-targeted nanoparticles was performed in U937 (human histiocytic lymphoma cell), which is one of the TSPO-overexpressed cell lines. The *in vitro* cell uptake experiments were conducted by means of confocal microscopy using human glioblastoma U87-MG cell lines in live mode and after immunofluorescence staining human fibroblast CCD-986sk fixed cells. Moreover, the correlation between inflammatory responses and TSPO expression at a cellular level was evaluated. The efficacy of the TSPO-targeted USPIONs *in vivo* as a tool for fluorescence imaging of GBM was assessed in 6-week-old male Balb/c athymic mice. Competition

studies were also performed *in vivo* using the selective TSPO ligand PK 11195.

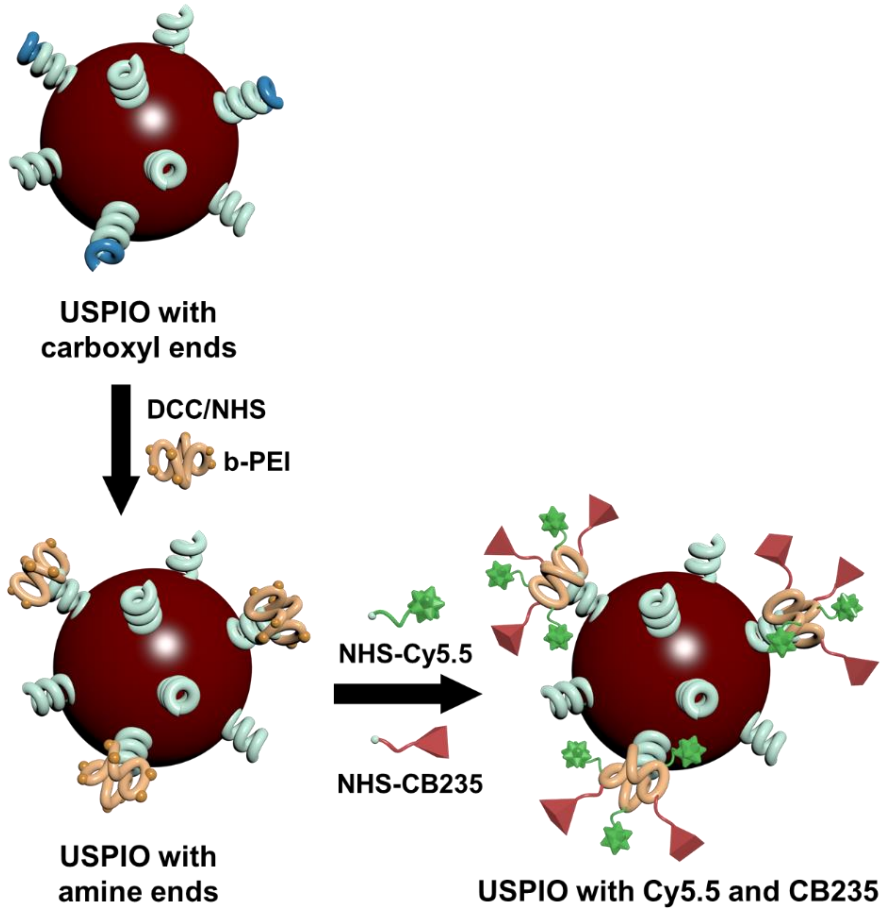

Figure 3.1 Schematic representation of Cy 5.5 and CB 235 labeling process for USPIONs.

3.2. Experimental

Materials

Ethylenediamine (EDA), branched polyethyleneimine (b-PEI, MW ~800), dicyclohexylcarbodiimide (DCC), N-Hydroxysuccinimide (NHS) and phosphate buffered saline (PBS) tablets were from Sigma Aldrich. Iron nitrate nonahydrate ($Fe(NO_3)_3 \cdot 9H_2O$), ethanol, polyethylene glycol (PEG, Mw ~600), dimethylsulfoxide and diethyl ether were purchased from Samchun Chemical (South Korea). Cyanine 5.5 dye (Flamma® 675 NHS ester) was bought from BioActs (South Korea). Other reagents were purchased from Sigma-Aldrich and Tokyo Chemical industry Co., Ltd. (TCI). All the reagents were used without further purification and aqueous solutions were prepared using high purity deionized water (18.2 MΩ).

Characterization

^{1}H- and ^{13}C-NMR spectra were recorded on a Varian at 400-MR (400 MHz) spectrometer (Agilent Technologies, USA). Chemical shifts were reported in parts per million (ppm, δ units). Electrospray mass spectrometry (ESI-MS) was performed on an LC/MS spectrometer (Agilent 6130 Series, Agilent Technologies, USA). High-Performance

Liquid Chromatography (HPLC) was carried out on a Dong-il Shimadzu Corp (Japan). Separation Products System equipped with a semi-preparative column (Waters, Xterra RP-C18, 10 μm, 10 × 250 mm) and equipped with a UV detector (wavelength set at 254 nm). HPLC-grade solvents (J. T. Baker, USA) were used for HPLC purification after filtering with a membrane filter (Whatman, 0.22 μm, USA). The HPLC eluent started with 65% acetonitrile and 35% water over 25 min at a flow rate of 4 mL per minutes. A fluorometer (Fluorolog 3, HORIBA Jobin-Yvon) was used for the quantitative analysis of the fluorescent dyes bound to the particles.

MR phantom test

Phantom images were obtained using a 9.4 T/160 AS animal MRI system (Agilent Technologies, Santa Clara, CA, USA). The transverse relaxation time T_2 mapping was estimated using MEMS (multi-echo multiple slices) sequences with a spin-echo readout. The sequence parameters were as follows: TR = 3000 ms, TE = 8.50 ms, NE = 16, average = 1, matrix size = 128 × 128, FOV (field of view) = 60.0 × 60.0 mm^2, slice thickness = 2.0 mm, and scan time = 6 min 30 s.

Synthesis of CB 235-NHS

NHS (14 mg, 0.12 mmol) and DCC (25 mg, 0.12 mmol) was added to 5 mL of dichloromethane containing 2-(4-(6,8-dichloro-3-(2-(dipropylamino)-2-oxoethyl)imidazo[1,2-a]pyridin-2-yl)phenoxy)acetic acid (CB 235, 50 mg, 0.10 mmol). The reaction mixture was stirred at room temperature for 4 h. The solvent was removed under reduced pressure and then the reaction mixture was dissolved in acetonitrile: water = 65:35 (v/v). The product was separated by a semi-preparative HPLC system. The fraction of CB 235-NHS was collected at 7.0 min as a white solid; ^{1}H-NMR (400 MHz, CDCl3) δ 8.29 (s, 1H), 7.63 (d, J = 8.8 Hz, 2H), 7.28 (s, 1H), 7.07 (d, J = 9.2 Hz, 2H), 5.02 (s, 2H), 4.05(s, 2H), 3.30 (t, J = 7.8 Hz, 2H), 3.11 (t, J = 7.8 Hz, 2H), 2.87 (s, 4H), 1.56-1.46 (m, 4H), 0.88-0.84 (m, 3H), 0.74-0.70 (m, 3H); ^{13}C-NMR (100 MHz, $CDCl_3$) δ 170.5, 167.1, 158.7, 140.6, 130.6, 125.9, 122.6, 121.7, 120.2, 117.3, 114.9, 65.5, 50.0, 48.2, 31.0, 30.0, 22.2, 20.9, 11.3, 11.1; MS (ESI) m/z 575.1($M+H^+$, 100%) 577.1(60%) 576.1(30%), 578.1(20%), 579.1(11%); ESI-MS m/z $C_{27}H_{29}O_6N_4Cl_2$ calculated: 575.1459; found: 575.1488.

One-step synthesis of water-dispersible ultra-small iron oxide nanoparticles (USPIONs)

The USPIONs in this research were reproduced following the previously reported method [105]. Typically, 1 mmol of ferric nitrate nonahydrate and 20 mmol of PEG 600 were transferred to 50 mL three-neck round bottom flask and degassed under 95 °C for 1 h. The color of the solution gradually changed to a deep reddish-brown color as it was heated. Then, the mixed solution was heated at 265 °C for 30 min to synthesize magnetite nanocrystals. A portion of the solution was mixed with a mixture of ethanol and ether and then purified by centrifugation. The procedure was repeated three times, and the purified nanoparticles were dispersed in the desired solvent and stored.

Surface functionalization of USPIONs with branched polyethyleneimine (b-PEI)

As mentioned in the previous paper [105], since the iron oxide nanoparticles synthesized by this method have a carboxyl group on the surface, in this study, the surface functionalization was processed through amide bonding formation. The purified nanoparticles (~ 8 mg) were redispersed in 2 mL of dimethylsulfoxide (DMSO), and each 1 mL

of dicyclohexylcarbodiimide (DCC) and N-hydroxysuccinimide (NHS) solution (0.1 M in DMSO) was added. After shaking for 30 min, 1 mL of b-PEI solution (1 wt.% in DMSO) was added to induce the reaction with NHS on the surface of the nanoparticles and the mixture was shaken for 4 h. Again, the nanoparticles were purified by centrifugation with a mixture of ethanol and ether and redispersed in ethanol for the next procedure.

Fluorescence labeling and TSPO-target ligand conjugation

Cyanine 5.5, a near-infrared fluorescent dye, was introduced on the surface of nanoparticles to reduce overlap of spectral absorbance by the iron oxide nanoparticles and to obtain a strong fluorescence image from the body. Both fluorescent dye and a CB 235 ligand, which had been pre-NHS-esterified at the end, were prepared and applied to the nanoparticles to facilitate attachment to the amine functional groups of the nanoparticles. 0.5 mmol of each was dissolved in 1 mL of ethanol and then added to an amine-functionalized iron oxide nanoparticle previously dispersed in 2 mL of ethanol, followed by shaking for 4 h. Unbound molecules were repeatedly centrifuged in the same manner as described above, and the nanoparticles were finally dispersed in a PBS

solution for *in vivo* experiments. In order to remove trace amounts of residual ether, the solution was purified through dialysis and prepared at a concentration of 1 $mgFe \cdot mL^{-1}$.

Cell lines

U87-MG (human malignant glioblastoma cell), U937 (human histiocytic lymphoma cell)and CCD-986sk (human fibroblast) were distributed from Korean Cell Line Bank (Seoul, Korea) and grown in Dulbecco's Modified Eagle's Medium (DMEM, SH30243.01; GE Healthcare, USA), Roswell Park Memorial Institute 1640 Medium (RPMI-1640, SH30027.01; GE Healthcare, USA) and Iscove's Modified Dulbecco's Medium (IMDM, SH30228.01; GE Healthcare, USA) respectively with 10% heat-activated fetal bovine serum (FBS, SH30919.03; GE Healthcare, USA) and 1% penicillin-streptomycin (15070-063; Life Technologies, USA). Cells were cultured at 37 °C in a humidified 5% CO_2 incubator.

***In vitro* toxicity test**

In vitro toxicity study of TSPO-targeted nanoparticles was performed in U937 (human histiocytic lymphoma cell), which is one of the TSPO-

overexpressed cell lines. This cell was cultured in a 12-well plate with 1 × 10^5 cells per well and different concentration of nanoparticles (0, 15, 30 and 60 μgFe·mL^{-1}). After incubating for 2, 4, 8 and 24 hr, cells were isolated from culture media and time-dependent viable cells was measured using cell counter (Countess II FL Automated Cell Counter; Life technologies, USA).

***In vitro* cellular uptake study**

About 5 × 10^4 U87-MG cells were seeded in 10 mm-cover glass-bottom dish as known as a confocal dish, 24 hr before for *in vitro* uptake study. Nanoparticles were treated with serum-containing media to the cells by 20 μgFe·mL^{-1} at 37 °C for 4 h. For cell nucleus and mitochondria staining, cells were soaked with 1× phosphate buffered saline (PBS) gently so as not to be detached. Shortly afterward, cells were incubated with Hoechst (H3570, 1:500; Life Technologies, USA) in serum-free medium at 37℃ for 20 min and then with 2 μM MitoTracker™ Green FM (M7514; Life Technologies, USA) under the same condition as Hoechst staining for 10 min. Cells were visualized by A1 Rsi Confocal Laser Scanning Microscope (Nikon, Japan) with ×60 magnification. PK

11195 was used as a blocking agent to test the targeting ability of the nanoparticles to the TSPO receptor.

***In vitro* immunofluorescence staining**

All the cells (U87-MG and CCD-986sk) were seeded in 10 mm-cover glass-bottom dish at a density of 5×10^4, 24 hr before immunofluorescence staining just the same as cellular uptake study. Nanoparticles were treated with serum-containing media to the cells by 20 $\mu gFe \cdot mL^{-1}$ at 37℃ for 4 h. The cells were fixed with 4% paraformaldehyde (PFA) for 20 min and then rinsed with PBS. After that, 0.2% Triton X-100 was treated into the cells for 15 min. For blocking of endogenous activity, the cells were placed with 4% bovine serum albumin (BSA) overnight at 4℃. These blocked cells were then incubated with PBR antibody (ab109497, 1:200; Abcam, Cambridge, UK) as a primary antibody in serum-free medium overnight at 4℃. After gently washing, a rabbit secondary antibody, Alexa fluor 488 (A11034, 1:1000; Life Technologies, CA, USA), was added into the cells and the cells were incubated for 1 h at 20-25 °C. Nuclear DNA was stained with Hoechst for 10 min. Stained cells were visualized by A1 Rsi Confocal Laser Scanning Microscope (Nikon, Japan) with ×60 magnification.

Animal models

6-week-old male Balb/c athymic mice were used in this *in vivo* experiment and those mice were purchased from Orient Biotech (Seoul, Korea). The animals were anesthetized with 2% isoflurane gas and 1×10^7 U87-MG cells with cold PBS were inoculated into forelimb armpit of mice (n=15) subcutaneously with a sterile 26-gauge needle. After 2 weeks, U87-MG xenograft models were obtained for imaging experiment. All the animals had been administered on a regular diet and all *in vivo* experiments were performed in accordance with the guidelines by Institutional Animal Care and Use Committee (IACUC) and Seoul National University Animal Care.

***In vivo* fluorescence imaging**

Animals were anesthetized by 2% isoflurane gas and 200 μgFe of nanoparticles were administered intravenously with an insulin syringe. *In vivo* fluorescence images were acquired at 30 min, 1 hr, 4 hr, 8 hr and 24 hr using *In Vivo* Imaging System (IVIS Lumina XRMS, CLS136340; Perkin Elmer, USA) with the indicated wavelength (excitation: 660 nm, emission: 710 nm). For blocking test, additional fluorescence imaging

was performed with the same protocol at 10 min after injection of PK 11195 (200 μg) to examine selective displacement of the nanoparticle to TSPO. Mice were kept alive and maintained body temperature at 37 °C during the imaging experiment. All images were analyzed by Image J open-source image processing software in terms of calculation of target-to-background (TBR).

3.3. Results and discussion

Synthesis and characterization of the TSPO ligand

The TSPO ligand was prepared prior to the synthesis of TSPO-targeted nanoparticles. This ligand contained a 2-phenylimidazo[1,2-a]pyridine acetamide structure was reported in our previous studies [19,20]. Especially, 2-(4-(6,8-dichloro-3-(2-(dipropylamino)-2-oxoethyl)imidazo[1,2-a]pyridin-2-yl)phenoxy)acetic acid (CB 235) has a high affinity and selectivity for TSPO [94,106,108]. In order to simply conjugate with iron oxide nanoparticle and CB 235, the CB 235-NHS was synthesized according to the scheme reported in **Figure 3.2**. The TSPO ligand CB 235 was treated in dichloromethane at room temperature with DCC and NHS. The desired compound was obtained in good yield (60%) and revealed an HPLC retention time of 7 min. The CB 235-NHS was characterized by ^{1}H-NMR and ^{13}C-NMR spectroscopy and ESI-MS.

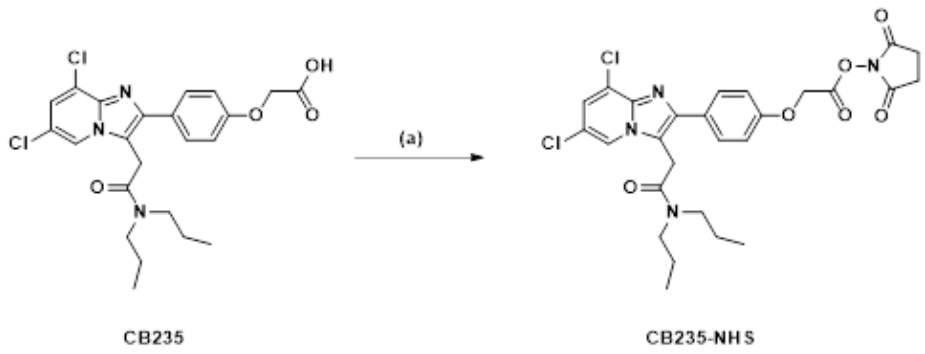

Figure 3.2 Synthesis of TSPO ligand: (a) NHS, DCC, DCM, r.t, 4hr.

Synthesis and characterization of USPIONs

The USPIONs synthesized using PEG as a solvent according to a previously reported method, purified by centrifugation, and then functionalized as shown in **Figure 3.1**. Some carboxyl groups on the surface of the synthesized USPIONs were allowed to bind the amine linker through a DCC / NHS coupling process and then branched PEI (b-PEI, MW ~800) was introduced to expand the reaction site. Considering the solubility of Cyanine 5.5 (Cy5.5) and CB 235, USPIONs activated on the surface of the amine was dispersed in ethanol and used in the next reaction. Cy5.5 dye and CB 235 ligand with NHS end were bound with simple stirring at room temperature. The modified USPIONs was observed to have an average diameter of about 5.57 nm through transmission electron microscopy, as shown in **Figure 3.3A** and **B**. A comparison of the hydrodynamic size of pristine USPIONs and modified USPIONs through DLS analysis showed an increase of about 2.6 nm (**Figure 3.3C**). As a result, it was confirmed that nanoparticles aggregation did not occur during the functionalization process and the added molecules were successfully introduced to the surface of USPIONs as expected.

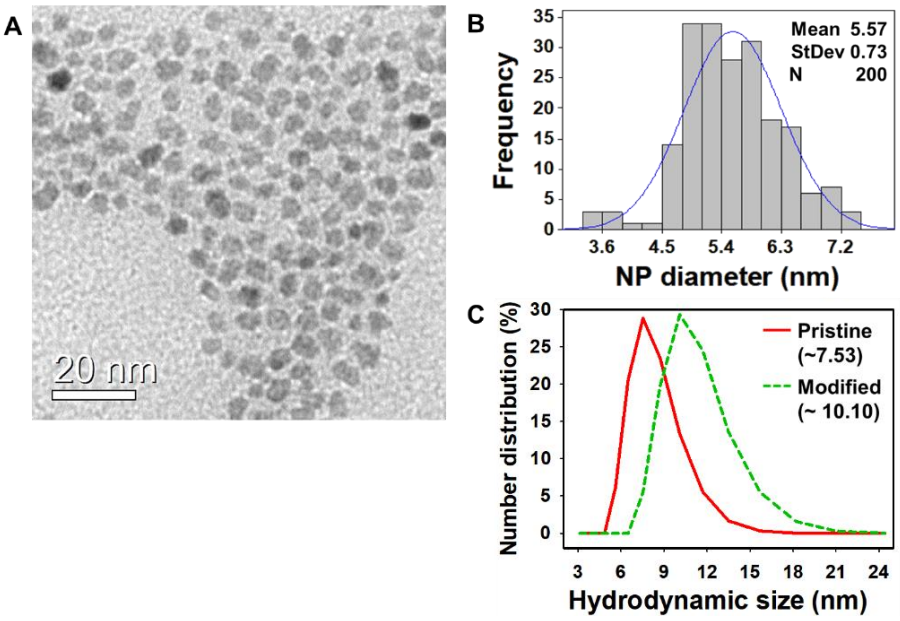

Figure 3.3 (A)TEM image of modified USPIONs and (B) their size distribution histogram. (C)Hydrodynamic size change between the pristine USPIONs and USPIONs after surface functionalization steps.

In this study, Cy 5.5, the near-infrared fluorescent dye, was combined to minimize spectral overlap with iron oxide nanoparticles. By comparing the fluorescence intensities according to the concentration of each of the fluorescent dyes and nanoparticles using a fluorometer, quantitative analysis of the fluorescent dyes bound to the particles was performed as shown in **Figure 3.4**. The results showed that about 722.9 nmol of fluorescent dye was bound per mg of nanoparticles. In case of the bifunctionally modified with TSPO ligand and the fluorescent dye at the same time, each moiety was fed in the ratio of 1:1, thus it was predicted that they were bound by about 361.4 nmol for each 1 mg of the nanoparticles.

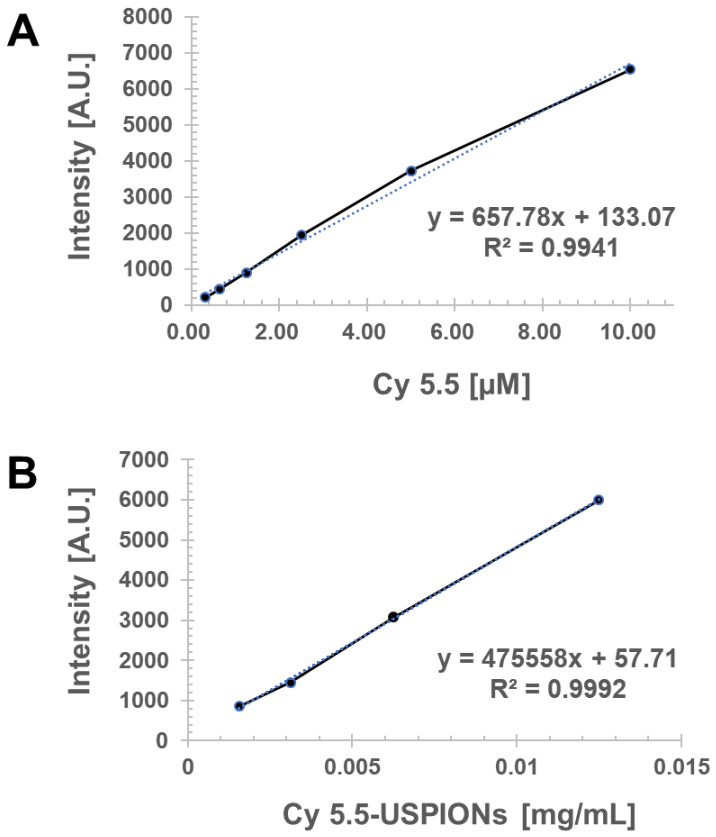

Figure 3.4 Standard curves of fluorescence intensity from (A) Cy 5.5 stock solutions and (B) Cy-5.5 labeled USPIONs colloidal solutions.

To verify the effect of the intermediate amine linker used for the introduction of fluorescent dyes, pristine USPIONs with two USPIONs obtained using EDA and b-PEI as linkers were prepared, respectively. As shown in **Figure 3.5A**, although the concentration of iron oxide nanoparticles was identical, deep green color, derived from the mixed color of iron oxide and Cy 5.5 dye, was most noticeable when b-PEI was used as the intermediate linker. Comparing the fluorescence intensity of each solution, it was observed that b-PEI could bind fluorescence dye more than EDA in terms of molecular structure (**Figure 3.5B**).

Since iron oxide nanoparticles not only provide a multifunctional platform surface but also serve as a contrast agent for acquiring MR images, a phantom test was performed to confirm T2 relaxation per iron concentration (**Figure 3.5C**).

In addition, the hydrodynamic size of nanoparticles dispersed in 0.01-0.1 M PBS was also measured for a month to assess the dispersion stability of modified USPIONs prior to *in vitro* and *in vivo* studies (**Figure 3.5D**). The hydrodynamic size was slightly larger in the 0.1 M PBS which was 10 times thicker than the isotonic solution, but the USPIONs was found to be dispersed well for a month without noticeable aggregation.

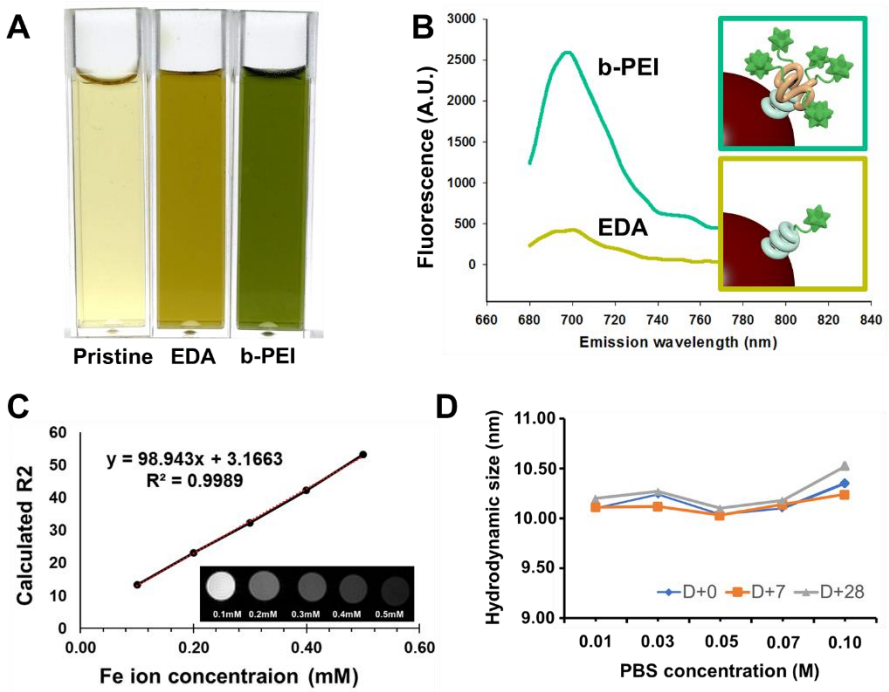

Figure 3.5 (A) Color change of USPIONs according to fluorescence dye attachment and (B) fluorescence intensity comparison of Cy 5.5-labeled USPIONs with EDA and b-PEI linker, respectively. (C) R2 relaxation rates as a function of iron concentration (mM) of NF-SIONs dispersed in DI water, measured at 25 °C and 9.4 T. Inset image represents T2-weighted MR enhancement of NF-SIONs in various concentration. (D) Hydrodynamic size change of USPIONs by 1-month DLS analysis.

In vitro toxicity and cellular uptake study

In vitro studies were carried out aimed first to assess the cytotoxicity of the nanoparticles and subsequently its ability to reach the intracellular target site on a panel of cell lines over-expressing the TSPO receptor such as U937 (human histiocytic lymphoma cell), U87-MG (human glioblastoma cancer cells). CCD-986sk (human fibroblast cells) were used as a negative model in the uptake experiments. The nanoparticles with both the fluorescent dye and the CB 235 ligand were designated as TSPO-targeted nanoparticles.

The toxicity of TSPO-targeted nanoparticles was evaluated in U937 cells. The number of viable cells after incubation with TSPO-targeted nanoparticles for 2, 4, 8 and 24 hr was registered with a cell counter and results are presented in **Figure 3.6**. As evidenced in the histogram the TSPO-targeted nanoparticles did not affect the cell proliferation either in terms of concentration or of time exposure. This can support the idea that this new targeted imaging nanoparticles may show no will be not cytotoxic for biomedical use.

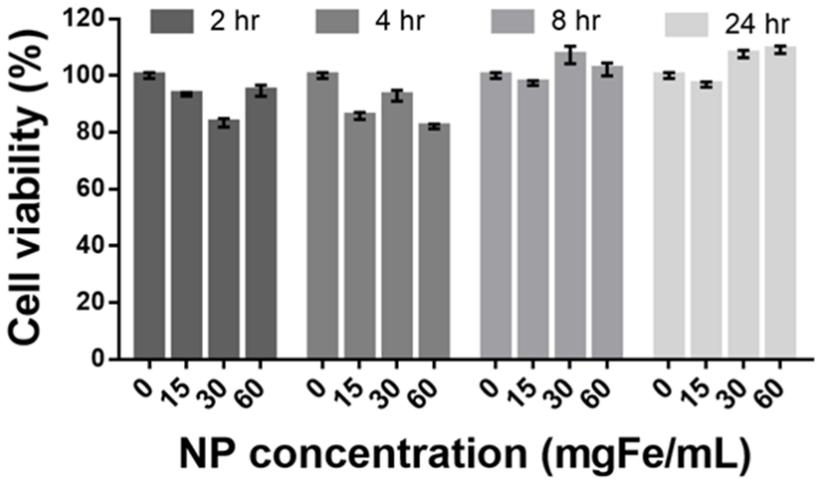

Figure 3.6 In vitro toxicity test of TSPO-targeted nanoparticles in different concentrations (0, 15, 30 and 60 $\mu g \cdot mL^{-1}$) using U937 cell line. Measurement of cell viability (%) was conducted at different time points (2, 4, 8 and 24 hr).

The cellular uptake and TSPO targeting pattern of TSPO-targeted nanoparticles were evaluated by *in vitro* immunofluorescence imaging using TSPO-overexpressing cell lines, U87-MG (glioblastoma) and TSPO-negative cell line, CCD-986sk (fibroblast). In particular, the nanoparticle localization analyses were conducted by means of confocal microscopy in live mode among U87-MG cells with and without the addition of TSPO-blocking agent, PK 11195 (**Figure 3.7**) and comparison with TSPO-negative cell line (CCD-986sk, **Figure 3.8**).

Confocal microscopy images obtained after incubation of U87-MG (**Figure 3.7D**) cells with TSPO-targeted nanoparticles clearly showed a comparable increase of the slightly aggregated orange merging patterns near the mitochondrial region, compared with the images obtained from PK 11195 treated cases (**Figure 3.7H**). The use of MitoTracker™ as a marker for exploring the behavior of nanoparticles targeting mitochondria has been suggested in several articles before, and locally clustered nanoparticles near the mitochondria as shown in **Figures 3.7D** were also observed in the references [111,112].

Although the exact uptake mechanism of the TSPO-targeted iron oxide nanoparticles has not been elucidated yet, it must be understood via one of the endocytosis-based pathways in order to target the

intracellular organelles rather than the cell surface [113]. In particular, when polycationic ligands such as PEI are bound to the surface of nanoparticles, they have been reported to cause disruption of the endosomal membrane and facilitate the endosomal escaping of nanoparticles [113,114].

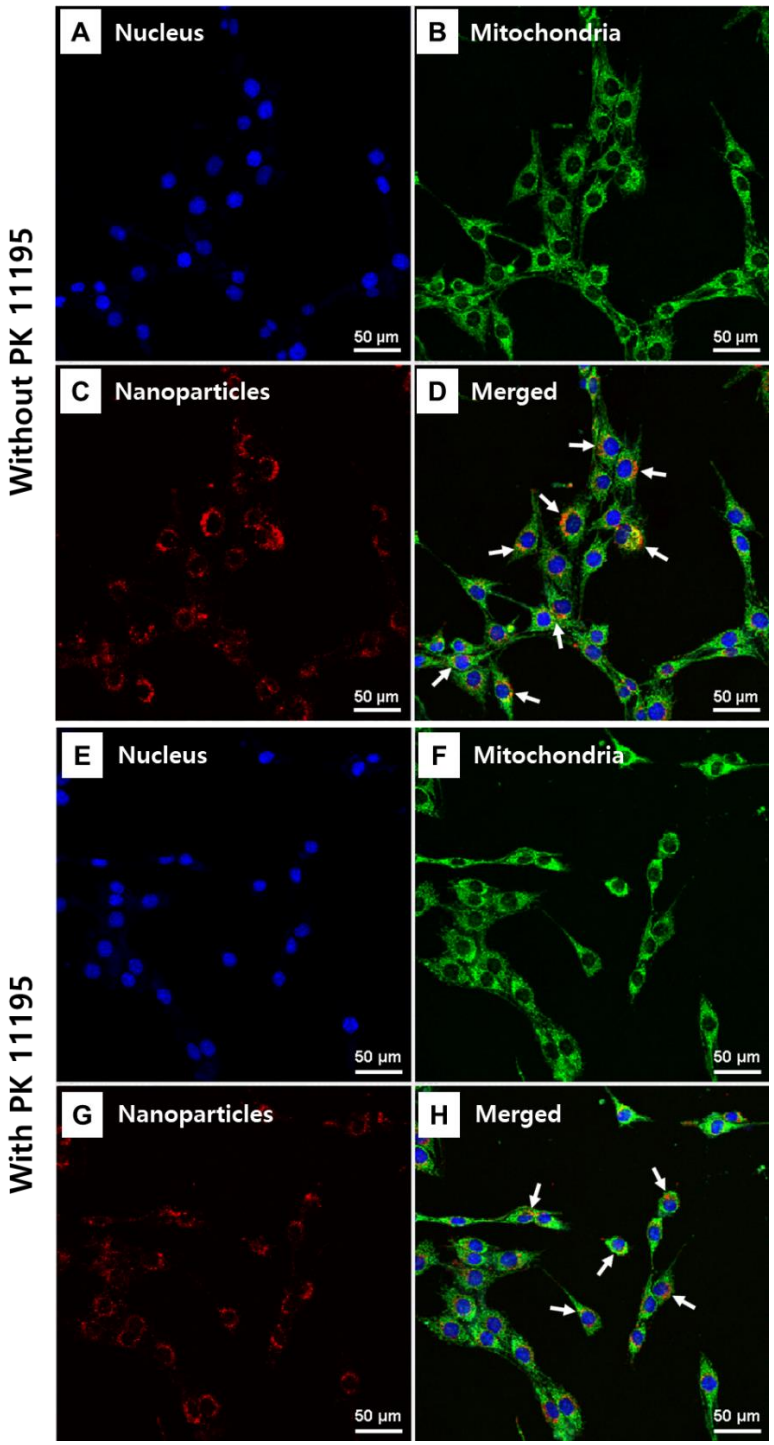
Without PK 11195
With PK 11195
A Nucleus
B Mitochondria
C Nanoparticles
D Merged
E Nucleus
F Mitochondria
G Nanoparticles
H Merged
50 µm

Figure 3.7 Immunofluorescence imaging of human glioblastoma cells U87-MG and TSPO-targeted nanoparticles (20 μg·mL^{-1}) without (A, B, C, and D) and with (E, F, G, and H) PK 11195 treatment. Green: mitochondria (MitoTracker™ Green FM), Blue: nucleus (DAPI), and Red: TSPO-targeted nanoparticles (Cy5.5). White arrows indicate merged signals of mitochondria and nanoparticles.

A comparison of U87-MG and CCD-986sk cells stained with mitochondria-specific antibody (Green), TSPO-targeted nanoparticles (Red) and nucleus staining dye (blue) confirms the results obtained in live mode on U87-MG cells (**Figure 3.8**), with a large merging area of red fluorescence of TSPO-targeted nanoparticles with the green fluorescence of the TSPO antibody (**Figure 3.8A**). However, such overlap was rarely observed in the negative model CCD-986sk (**Figure 3.8B**).

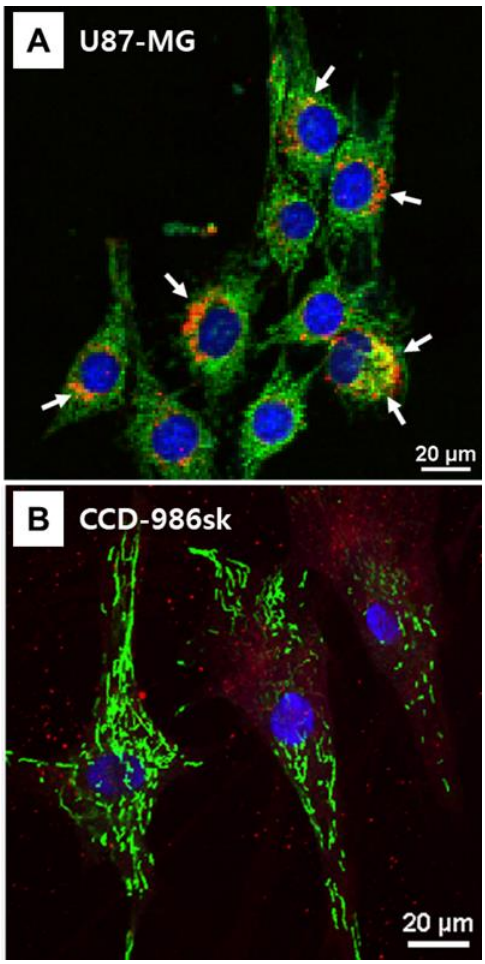

Figure 3.8 Confocal microscopy images of two cell lines; glioblastoma cells and human fibroblast cells stained with mitochondria-specific antibody (Green), TSPO-targeted nanoparticles (Red), and nucleus staining dye (blue, Hoechst). (A) U87-MG (glioblastoma cells) as a positive control with TSPO-targeted nanoparticles and (B) CCD-986sk (Human fibroblast cells) as a negative control with TSPO-targeted nanoparticles.

In vivo fluorescence imaging

After a preliminary *in vitro* evaluation of the ability of TSPO-targeted nanoparticles to recognize the intracellular receptor TSPO, in order to assess their ability as new fluorescence imaging agents of GBM, *in vivo* experiments on U87-MG xenograft models obtained from 6-week-old male Balb/c athymic mice were performed, by pre-injecting the TSPO selective ligand PK 11195 before proceeding with administration of the TSPO-targeted nanoparticles. As shown in **Figure 3.9**, the signal associated with the targeted nanoparticles, for every time post-injection considered, was much more intense in the absence of PK 11195 (**Figure 3.9A**) than in the presence (**Figure 3.9B**). These data were represented in a graph reported in **Figure 3.9C** as a tumor-to-skin-ratio, from which the displacement capacity of PK 11195 by TSPO-targeted nanoparticles was quantitatively demonstrated. This also confirmed the ability of the newly prepared imaging nanoparticles to reach *in vivo* the tumor target site. Moreover, in **Figure 3.10**, the organ distribution of TSPO-targeted nanoparticles was reported in both conditions mentioned above and the shown images clearly represent a preferential distribution of nanoparticles at the tumor site.

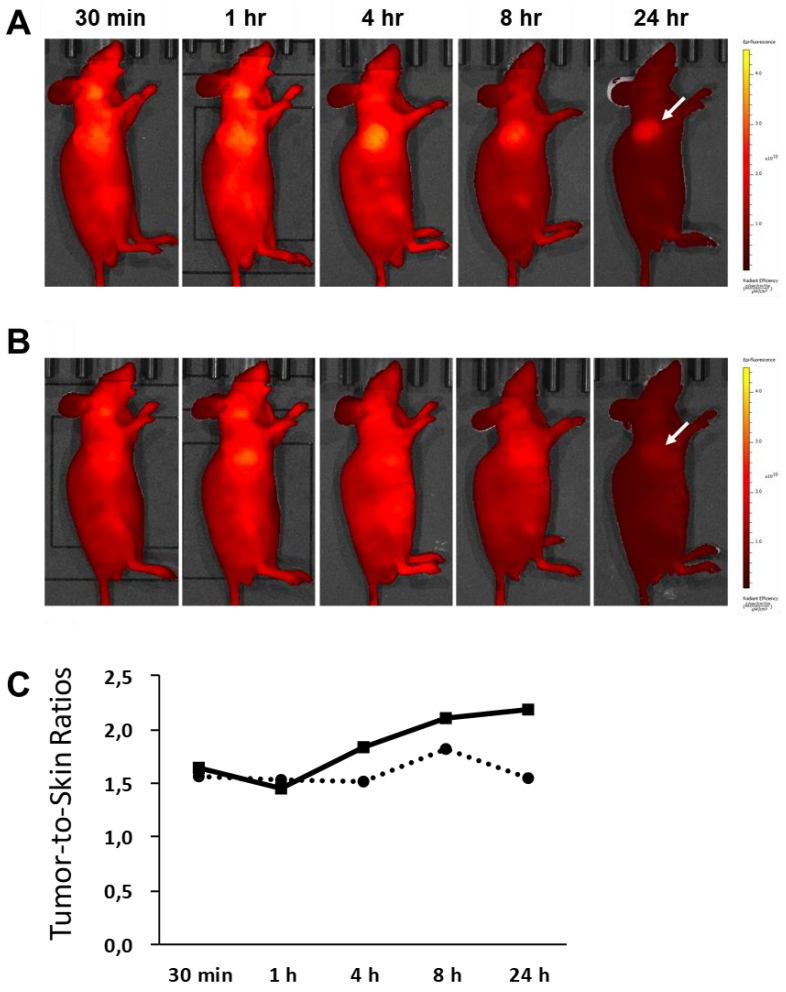

Figure 3.9 Fluorescence imaging study by IVIS Lumina XRMS. (A) Imaging of U87-MG xenograft model at 30 min, 1 hr, 4 hr, 8 hr, and 24 hr post-injection of TSPO-targeted nanoparticle (200 μgFe). (B) Inhibition study using PK 11195 (10 mg per 1 kg). (C)Tumor-to-skin ratios in mouse models with PK 11195 pre-injection or without PK 11195 pre-injection.

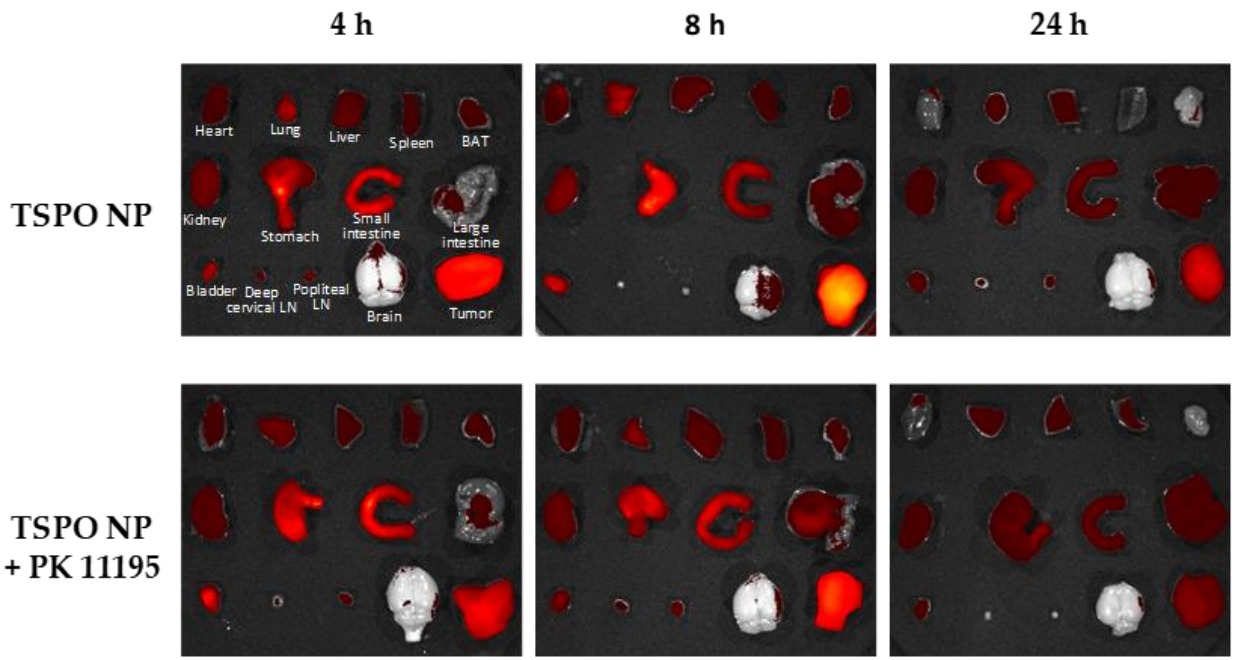

Figure 3.10 Observation of fluorescence change according to time and PK 11195 injection in each organ resected from nanoparticles-injected tumor-bearing models.

3.4. Summary

The water-dispersible ultra-small iron oxide nanoparticles (USPIONs) were synthesized in one step and conjugated with Cyanine 5.5, a near-infrared fluorescent dye, and with a ligand that specifically targeting TSPO, in order to realize a new NIR fluorescent nanoprobe as an *in vivo* tool for fluorescence imaging of GBM. It was confirmed that the new TSPO-targeted imaging nanoprobe shows high colloidal stability in physiological media and preserves the relevant optical properties in the NIR region even after conjugation with the TSPO ligand. The confocal microscopy imaging demonstrated the cellular internalization and TSPO binding of the fed USPIONs among the several cell lines that are known to overexpress the TSPO receptor. The ability to recognize the intracellular receptor was confirmed *in vivo* by competition studies with the selective TSPO ligand PK 11195. Moreover, the images of U87-MG xenograft models administered with TSPO-targeted nanoparticles and acquired with x-ray multi-species optical imaging system evidenced their effectiveness in the visualization of the tumor site. Thus, the proposed novel imaging system holds great promise as optical TSPO-targeted nanoparticles for *in vivo* NIR molecular imaging applications.

Chapter 4.

Conclusions

In summary, this study mainly focused on the surface processing of iron oxide nanoparticles and multifunctionalization strategies such as fluorescence, dispersibility, and target specificity for precision cancer imaging.

First, the dual-modal nanoparticles capable of simultaneous MR/fluorescence imaging were synthesized by reverse microemulsion method with two-step silanization for minimization of spectral overlap between the iron oxide nanoparticles and introduced fluorescent dyes. The long-term dispersion stability was verified in a body fluid-like environment so that it could penetrate well into the tumor microenvironment without aggregation via intravenous administration. The distribution of nanoparticles at the cellular and animal level was confirmed by immunofluorescence analysis and suggested the potential as a functional contrast agent for comprehensive tumor resection in fluorescence-guided surgery based on interaction with tumor microenvironmental components.

Second, a novel strategy was developed to produce dual-modal MR/fluorescence imaging nanoparticles targeting TSPO ligands, which is recently studied as a biomarker of brain tumors and neural diseases, as well as inflammatory macrophages, and verified targeting specificity of

synthesized nanoparticles for cancer cells and adjacent tissues. By introducing the branch structured intermediate linker, the amount of ligand bound to the nanoparticle surface was effectively increased, and the change in physicochemical properties was confirmed with a slight increase in hydrodynamic size. Besides, quantitative fluorescence analysis of TSPO-targeted nanoparticles accumulated at adjacent tumor sites was conducted using a competitive inhibitor that acts as a TSPO blocking agent.

Throughout the whole studies, the targeting ability of functionalized nanoparticles against the tumor-related components and systematic immunofluorescence analyses in tumor-bearing mouse models were conducted for providing their potentials as multifunctional nanoprobes for precision cancer imaging applications. However, it is considered that the limitation of this study is the fact that the whole-body MR image was not confirmed in the tumor model even though iron oxide nanoparticles were used as the essential nanoplatform.

Although there are lots of basic studies on the nanoparticle-specific uptake of tumor-associated macrophages and researches concerning TSPO as a cancer biomarker are actively underway, most of the studies are still at pre-clinical levels in animal models. However, if there is a

continuing interest in basic research on the interaction of nanoparticles in terms of their surface chemical properties and on diagnostic and therapeutic applications in the tumor microenvironment, significant progress will be made in the clinical management of intractable brain tumors.

References

1. K. Ariga, Q. Ji, W. Nakanishi, J. P. Hill, and M. Aono, Mater. Horizons **2**, 406 (2015).

2. A. Wicki, D. Witzigmann, V. Balasubramanian, and J. Huwyler, J. Control. Release **200**, 138 (2015).

3. *National Cancer Center* (2016).

4. J. K. L. Wong, R. Mohseni, A. A. Hamidieh, R. E. MacLaren, N. Habib, and A. M. Seifalian, Trends Biotechnol. **35**, 434 (2017).

5. G. Minniti, V. De Sanctis, R. Muni, F. Filippone, A. Bozzao, M. Valeriani, M. F. Osti, U. De Paula, G. Lanzetta, V. Tombolini, and R. Maurizi Enrici, J. Neurooncol. **88**, 97 (2008).

6. J. A. Bonner, P. M. Harari, J. Giralt, N. Azarnia, D. M. Shin, R. B. Cohen, C. U. Jones, R. Sur, D. Raben, J. Jassem, R. Ove, M. S. Kies, J. Baselga, H. Youssoufian, N. Amellal, E. K. Rowinsky, and K. K. Ang, N. Engl. J. Med. **354**, 567 (2006).

7. J. S. Cooper, T. F. Pajak, A. A. Forastiere, J. Jacobs, B. H. Campbell, S. B. Saxman, J. A. Kish, H. E. Kim, A. J. Cmelak, M. Rotman, M. Machtay, J. F. Ensley, K. S. C. Chao, C. J. Schultz, N. Lee, and K. K. Fu, N. Engl. J. Med. **350**, 1937 (2004).

8. A. A. Forastiere, H. Goepfert, M. Maor, T. F. Pajak, R. Weber, W. Morrison, B. Glisson, A. Trotti, J. A. Ridge, C. Chao, G. Peters, D.-J. Lee, A. Leaf, J. Ensley, and J. Cooper, N. Engl. J. Med. **349**, 2091 (2003).

9. M. Al-Sarraf, M. LeBlanc, P. G. Giri, K. K. Fu, J. Cooper, T. Vuong, A. A. Forastiere, G. Adams, W. A. Sakr, D. E. Schuller, and J. F. Ensley, J. Clin. Oncol. **16**, 1310 (1998).

10. W. Sause, P. Kolesar, S. Taylor, D. Johnson, R. Livingston, R. Komaki, B. Emami, W. Curran, R. Byhardt, A. R. Dar, and A. Turrisi, Chest **117**, 358 (2000).

11. R. Komaki, C. B. Scott, W. T. Sause, D. H. Johnson, S. G. Taylor, J. S. Lee, B. Emami, R. W. Byhardt, W. J. Curran, A. R. Dar, and J. D. Cox, Int. J. Radiat. Oncol. **39**, 537 (1997).

12. B. D. Minsky, T. F. Pajak, R. J. Ginsberg, T. M. Pisansky, J. Martenson, R. Komaki, G. Okawara, S. A. Rosenthal, and D. P. Kelsen, J. Clin. Oncol. **20**, 1167 (2002).

13. A. W. Fyles, D. R. McCready, L. A. Manchul, M. E. Trudeau, P. Merante, M. Pintilie, L. M. Weir, and I. A. Olivotto, N. Engl. J. Med. **351**, 963 (2004).

14. J. Ragaz, I. A. Olivotto, J. J. Spinelli, N. Phillips, S. M. Jackson, K. S. Wilson, M. A. Knowling, C. M. L. Coppin, L. Weir, K. Gelmon, N.

Le, R. Durand, A. J. Coldman, and M. Manji, JNCI J. Natl. Cancer Inst. **97**, 116 (2005).

15. W. F. Regine, K. A. Winter, R. A. Abrams, H. Safran, J. P. Hoffman, A. Konski, A. B. Benson, J. S. Macdonald, M. R. Kudrimoti, M. L. Fromm, M. G. Haddock, P. Schaefer, C. G. Willett, and T. A. Rich, JAMA **299**, 1019 (2008).

16. M. Morris, P. J. Eifel, J. Lu, P. W. Grigsby, C. Levenback, R. E. Stevens, M. Rotman, D. M. Gershenson, and D. G. Mutch, N. Engl. J. Med. **340**, 1137 (1999).

17. R. Sauer, H. Becker, W. Hohenberger, C. Rödel, C. Wittekind, R. Fietkau, P. Martus, J. Tschmelitsch, E. Hager, C. F. Hess, J.-H. Karstens, T. Liersch, H. Schmidberger, and R. Raab, N. Engl. J. Med. **351**, 1731 (2004).

18. B. Vikram, C. N. Coleman, and J. A. Deye, Oncology (Williston Park). **23**, 380 (2009).

19. D. Hanahan and R. A. Weinberg, Cell **144**, 646 (2011).

20. F. Chen, X. Zhuang, L. Lin, P. Yu, Y. Wang, Y. Shi, G. Hu, and Y. Sun, BMC Med. **13**, 45 (2015).

21. M. Labelle and R. O. Hynes, Cancer Discov. **2**, 1091 (2012).

22. K. Glunde, C. A. Foss, and Z. M. Bhujwalla, Biomed. Inf. Technol. **312**, 431 (2008).

23. D. E. Lee, H. Koo, I. C. Sun, J. H. Ryu, K. Kim, and I. C. Kwon, Chem. Soc. Rev. **41**, 2656 (2012).

24. E. L. Ritman, Annu. Rev. Biomed. Eng. **6**, 185 (2004).

25. J. C. Richardson, R. W. Bowtell, K. Mäder, and C. D. Melia, Adv. Drug Deliv. Rev. **57**, 1191 (2005).

26. A. B. Chinen, C. M. Guan, J. R. Ferrer, S. N. Barnaby, T. J. Merkel, and C. A. Mirkin, Chem. Rev. **115**, 10530 (2015).

27. J. K. Willmann, N. van Bruggen, L. M. Dinkelborg, and S. S. Gambhir, Nat. Rev. Drug Discov. **7**, 591 (2008).

28. A. Louie, Chem. Rev. **110**, 3146 (2010).

29. L. E. Jennings and N. J. Long, Chem. Commun. 3511 (2009).

30. N. Lee, H. R. Cho, M. H. Oh, S. H. Lee, K. Kim, B. H. Kim, K. Shin, T. Y. Ahn, J. W. Choi, Y. W. Kim, S. H. Choi, and T. Hyeon, J. Am. Chem. Soc. **134**, 10309 (2012).

31. M. H. Oh, N. Lee, H. Kim, S. P. Park, Y. Piao, J. Lee, S. W. Jun, W. K. Moon, S. H. Choi, and T. Hyeon, J. Am. Chem. Soc. **133**, 5508 (2011).

32. X. Yang, H. Hong, J. J. Grailer, I. J. Rowland, A. Javadi, S. A. Hurley, Y. Xiao, Y. Yang, Y. Zhang, R. J. Nickles, W. Cai, D. A. Steeber, and S. Gong, Biomaterials **32**, 4151 (2011).

33. H.-Y. Lee, Z. Li, K. Chen, A. R. Hsu, C. Xu, J. Xie, S. Sun, and X. Chen, J. Nucl. Med. **49**, 1371 (2008).

34. T. Nam, S. Park, S. Y. Lee, K. Park, K. Choi, I. C. Song, M. H. Han, J. J. Leary, S. A. Yuk, I. C. Kwon, K. Kim, and S. Y. Jeong, Bioconjug. Chem. **21**, 578 (2010).

35. D. Yoo, C. Lee, B. Seo, and Y. Piao, RSC Adv. **7**, 12876 (2017).

36. T. Chanmee, P. Ontong, K. Konno, and N. Itano, Cancers (Basel). **6**, 1670 (2014).

37. L. Yang and Y. Zhang, J. Hematol. Oncol. **10**, 58 (2017).

38. S. Vinogradov, G. Warren, and X. Wei, Nanomedicine **9**, 695 (2014).

39. M. Preusser, S. De Ribaupierre, A. Wöhrer, S. C. Erridge, M. Hegi, M. Weller, and R. Stupp, Ann. Neurol. **70**, 9 (2011).

40. M. Lorger, Cancers (Basel). **4**, 218 (2012).

41. D. Hambardzumyan, D. H. Gutmann, and H. Kettenmann, Nat. Neurosci. **19**, 20 (2015).

42. Z. Chen, X. Feng, C. J. Herting, V. A. Garcia, K. Nie, W. W. Pong, R. Rasmussen, B. Dwivedi, S. Seby, S. A. Wolf, D. H. Gutmann, and D. Hambardzumyan, Cancer Res. **77**, 2266 (2017).

43. S. G. M. Piccirillo, S. Dietz, B. Madhu, J. Griffiths, S. J. Price, V. P. Collins, and C. Watts, Br. J. Cancer **107**, 462 (2012).

44. M. J. Landau, D. J. Gould, and K. M. Patel, Ann. Transl. Med. **4**, 392 (2016).

45. D. A. Hansen, A. M. Spence, T. Carski, and M. S. Berger, Surg. Neurol. **40**, 451 (1993).

46. J. T. Senders, I. S. Muskens, R. Schnoor, A. V. Karhade, D. J. Cote, T. R. Smith, and M. L. D. Broekman, Acta Neurochir. (Wien). **159**, 151 (2017).

47. C. Wang, Z. Wang, T. Zhao, Y. Li, G. Huang, B. D. Sumer, and J. Gao, Biomaterials **157**, 62 (2018).

48. S. Shimizu, W. Kamiike, N. Hatanaka, Y. Yoshida, K. Tagawa, M. Miyata, and H. Matsuda, World J. Surg. **19**, 113 (1995).

49. R. Tréhin, J.-L. Figueiredo, M. J. Pittet, R. Weissleder, L. Josephson, and U. Mahmood, Neoplasia **8**, 302 (2006).

50. C. M. McCann, P. Waterman, J. L. Figueiredo, E. Aikawa, R. Weissleder, and J. W. Chen, Neuroimage **45**, 360 (2009).

51. M. R. Pickard and D. M. Chari, Int. J. Mol. Sci. **11**, 967 (2010).

52. D. Ni, J. Zhang, W. Bu, H. Xing, F. Han, Q. Xiao, Z. Yao, F. Chen, Q. He, J. Liu, S. Zhang, W. Fan, L. Zhou, W. Peng, and J. Shi, ACS Nano **8**, 1231 (2014).

53. D. Alizadeh, L. Zhang, J. Hwang, T. Schluep, and B. Badie, Nanomedicine Nanotechnology, Biol. Med. **6**, 382 (2010).

54. Q. Fan, K. Cheng, Z. Yang, R. Zhang, M. Yang, X. Hu, X. Ma, L. Bu, X. Lu, X. Xiong, W. Huang, H. Zhao, and Z. Cheng, Adv. Mater. **27**, 774 (2015).

55. D. A. Orringer, Y. E. L. Koo, T. Chen, G. Kim, H. J. Hah, H. Xu, S. Wang, R. Keep, M. A. Philbert, R. Kopelman, and O. Sagher, Neurosurgery **64**, 965 (2009).

56. T. Nann and P. Mulvaney, Angew. Chemie - Int. Ed. **43**, 5393 (2004).

57. D. K. Yi, S. T. Selvan, S. S. Lee, G. C. Papaefthymiou, D. Kundaliya, and J. Y. Ying, J. Am. Chem. Soc. **127**, 4990 (2005).

58. H. Jang, C. Lee, G. E. Nam, B. Quan, H. J. Choi, J. S. Yoo, and Y. Piao, J. Nanoparticle Res. **18**, 1 (2016).

59. D. R. Larson, H. Ow, H. D. Vishwasrao, A. A. Heikal, U. Wiesner, and W. W. Webb, Chem. Mater. **20**, 2677 (2008).

60. A. Burns, H. Ow, and U. Wiesner, Chem. Soc. Rev. **35**, 1028 (2006).

61. M. F. Kircher, U. Mahmood, R. S. King, R. Weissleder, and L. Josephson, Cancer Res. **63**, 8122 (2003).

62. W. Cai, D. W. Shin, K. Chen, O. Gheysens, Q. Cao, S. X. Wang, S. S. Gambhir, and X. Chen, Nano Lett. **6**, 669 (2006).

63. H. Jackson, O. Muhammad, H. Daneshvar, J. Nelms, A. Popescu, M. A. Vogelbaum, M. Bruchez, and S. A. Toms, Neurosurgery **60**, 524 (2007).

64. L. Jiang, Q. Zhou, K. Mu, H. Xie, Y. Zhu, W. Zhu, Y. Zhao, H. Xu, and X. Yang, Biomaterials **34**, 7418 (2013).

65. L. Cui, Q. Lin, C. S. Jin, W. Jiang, H. Huang, L. Ding, N. Muhanna, J. C. Irish, F. Wang, J. Chen, and G. Zheng, ACS Nano **9**, 4484 (2015).

66. S. Sun, H. Zeng, D. B. Robinson, S. Raoux, P. M. Rice, S. X. Wang, and G. Li, J. Am. Chem. Soc. **126**, 273 (2004).

67. H. L. Ding, Y. X. Zhang, S. Wang, J. M. Xu, S. C. Xu, and G. H. Li, Chem. Mater. **24**, 4572 (2012).

68. A. Bumb, C. A. S. Regino, M. R. Perkins, M. Bernardo, M. Ogawa, L. Fugger, P. L. Choyke, P. J. Dobson, and M. W. Brechbiel, Nanotechnology **21**, 175704 (2010).

69. J. I. Kuroda, J. I. Kuratsu, M. Yasunaga, Y. Koga, Y. Saito, and Y. Matsumura, Int. J. Cancer **124**, 2505 (2009).

70. B. R. Renikuntla, H. C. Rose, J. Eldo, A. S. Waggoner, and B. A. Armitage, Org. Lett. **6**, 909 (2004).

71. E. S. Jang, S. Y. Lee, E. J. Cha, I. C. Sun, I. C. Kwon, D. Kim, Y. Il Kim, K. Kim, and C. H. Ahn, Pharm. Res. **31**, 3371 (2014).

72. J. Xie, C. Xu, N. Kohler, Y. Hou, and S. Sun, Adv. Mater. **19**, 3163 (2007).

73. Y. H. Lien and T. M. Wu, J. Colloid Interface Sci. **326**, 517 (2008).

74. D. Yoo, C. Lee, B. Seo, and Y. Piao, RSC Adv. **7**, 12876 (2017).

75. G. Kandasamy and D. Maity, Int. J. Pharm. **496**, 191 (2015).

76. L. C. J. Thomassen, A. Aerts, V. Rabolli, D. Lison, L. Gonzalez, M. Kirsch-Volders, D. Napierska, P. H. Hoet, C. E. A. Kirschhock, and J. A. Martens, Langmuir **26**, 328 (2010).

77. M. A. Malvindi, V. De Matteis, A. Galeone, V. Brunetti, G. C. Anyfantis, A. Athanassiou, R. Cingolani, and P. P. Pompa, PLoS One **9**, e85835 (2014).

78. U. Prabhakar, H. Maeda, R. K. Jain, E. M. Sevick-Muraca, W. Zamboni, O. C. Farokhzad, S. T. Barry, A. Gabizon, P. Grodzinski, and D. C. Blakey, Cancer Res. **73**, 2412 (2013).

79. H. Maeda, Adv. Enzyme Regul. **41**, 189 (2001).

80. A. Rodzinski, R. Guduru, P. Liang, A. Hadjikhani, T. Stewart, E. Stimphil, C. Runowicz, R. Cote, N. Altman, R. Datar, and S. Khizroev, Sci. Rep. **6**, 20867 (2016).

81. F. Danhier, O. Feron, and V. Préat, J. Control. Release **148**, 135 (2010).

82. Y. Zhou, Z. Peng, E. S. Seven, and R. M. Leblanc, J. Control. Release **270**, 290 (2018).

83. S. Watkins, S. Robel, I. F. Kimbrough, S. M. Robert, G. Ellis-Davies, and H. Sontheimer, Nat. Commun. **5**, 4196 (2014).

84. L. G. Dubois, L. Campanati, C. Righy, I. D'Andrea-Meira, T. C. L. de S. E. Spohr, I. Porto-Carreiro, C. M. Pereira, J. Balça-Silva, S. A. Kahn, M. F. DosSantos, M. de A. R. Oliveira, A. Ximenes-da-Silva, M. C. Lopes, E. Faveret, E. L. Gasparetto, and V. Moura-Neto, Front. Cell. Neurosci. **8**, 418 (2014).

85. J. N. Sarkaria, L. S. Hu, I. F. Parney, D. H. Pafundi, D. H. Brinkmann, N. N. Laack, C. Giannini, T. C. Burns, S. H. Kizilbash, J. K. Laramy, K. R. Swanson, T. J. Kaufmann, P. D. Brown, N. Y. R. Agar, E. Galanis, J. C. Buckner, and W. F. Elmquist, Neuro. Oncol. **20**, 184 (2018).

86. H. Wolburg, S. Noell, P. Fallier-Becker, A. F. MacK, and K. Wolburg-Buchholz, Mol. Aspects Med. **33**, 579 (2012).

87. E. Phillips, O. Penate-Medina, P. B. Zanzonico, R. D. Carvajal, P. Mohan, Y. Ye, J. Humm, M. Gönen, H. Kalaigian, H. Schöder, H. W. Strauss, S. M. Larson, U. Wiesner, and M. S. Bradbury, Sci. Transl. Med. **6**, 260ra149 (2014).

88. R. M. Iacobazzi, A. Lopalco, A. Cutrignelli, V. Laquintana, A. Lopedota, M. Franco, and N. Denora, ChemMedChem **12**, 1261 (2017).

89. S. Savino, N. Denora, R. M. Iacobazzi, L. Porcelli, A. Azzariti, G. Natile, and N. Margiotta, Int. J. Mol. Sci. **17**, 1010 (2016).

90. S. Piccinonna, N. Margiotta, N. Denora, R. M. Iacobazzi, C. Pacifico, G. Trapani, and G. Natile, Dalt. Trans. **42**, 10112 (2013).

91. G. F. Mangiatordi, D. Trisciuzzi, D. Alberga, N. Denora, R. M. Iacobazzi, D. Gadaleta, M. Catto, and O. Nicolotti, Eur. J. Med. Chem. **139**, 792 (2017).

92. A. Lopalco, A. Cutrignelli, N. Denora, M. Perrone, R. M. Iacobazzi, E. Fanizza, A. Lopedota, N. Depalo, M. De Candia, M. Franco, and V. Laquintana, Int. J. Mol. Sci. **19**, 1155 (2018).

93. M. Perrone, B. S. Moon, H. S. Park, V. Laquintana, J. H. Jung, A. Cutrignelli, A. Lopedota, M. Franco, S. E. Kim, B. C. Lee, and N. Denora, Sci. Rep. **6**, 20422 (2016).

94. A. Midzak, N. Denora, V. Laquintana, A. Cutrignelli, A. Lopedota, M. Franco, C. D. Altomare, and V. Papadopoulos, Eur. J. Pharm. Sci. **76**, 231 (2015).

95. S. Piccinonna, N. Margiotta, C. Pacifico, A. Lopalco, N. Denora, S. Fedi, M. Corsini, and G. Natile, Dalt. Trans. **41**, 9689 (2012).

96. R. M. Iacobazzi, P. Letizia, L. A. Assunta, L. Valentino, L. Antonio, C. Annalisa, A. Emiliano, D. F. Roberta, A. Amalia, F. Massimo, and D. Nunzio, Int. J. Pharm. **528**, 485 (2017).

97. J. Y. Choi, R. M. Iacobazzi, M. Perrone, N. Margiotta, A. Cutrignelli, J. H. Jung, D. D. Park, B. S. Moon, N. Denora, S. E. Kim, and B. C. Lee, Int. J. Mol. Sci. **17**, 1085 (2016).

98. N. Denora, R. M. Iacobazzi, G. Natile, and N. Margiotta, Coord. Chem. Rev. **341**, 1 (2017).

99. V. Laquintana, N. Denora, A. Cutrignelli, M. Perrone, R. Iacobazzi, C. Annese, A. Lopalco, A. Lopedota, and M. Franco, Int. J. Mol. Sci. **17**, 967 (2016).

100. A. Elkamhawy, A. N. I. Viswanath, A. N. Pae, H. Y. Kim, J. C. Heo, W. K. Park, C. O. Lee, H. Yang, K. H. Kim, D. H. Nam, H. J. Seol, H. Cho, and E. J. Roh, Eur. J. Med. Chem. **103**, 210 (2015).

101. T. Cassano, A. Lopalco, M. De Candia, V. Laquintana, A. Lopedota, A. Cutrignelli, M. Perrone, R. M. Iacobazzi, G. Bedse, M. Franco, N. Denora, and C. D. Altomare, Mol. Pharm. **14**, 3178 (2017).

102. B. Halamoda Kenzaoui, S. Angeloni, T. Overstolz, P. Niedermann, C. Chapuis Bernasconi, M. Liley, and L. Juillerat-Jeanneret, ACS Appl. Mater. Interfaces **5**, 3581 (2013).

103. A. Lopalco, H. Ali, N. Denora, and E. Rytting, Int. J. Nanomedicine **10**, 1985 (2015).

104. N. Depalo, R. M. Iacobazzi, G. Valente, I. Arduino, S. Villa, F. Canepa, V. Laquintana, E. Fanizza, M. Striccoli, A. Cutrignelli, A. Lopedota, L. Porcelli, A. Azzariti, M. Franco, M. L. Curri, and N. Denora, Nano Res. **10**, 2431 (2017).

105. K. M. Yang, H. Il Cho, H. J. Choi, and Y. Piao, J. Mater. Chem. B **2**, 3355 (2014).

106. N. Denora, V. Laquintana, A. Lopalco, R. M. Iacobazzi, A. Lopedota, A. Cutrignelli, G. Iacobellis, C. Annese, M. Cascione, S. Leporatti, and M. Franco, J. Control. Release **172**, 1111 (2013).

107. N. Denora, V. Laquintana, M. G. Pisu, R. Dore, L. Murru, A. Latrofa, G. Trapani, and E. Sanna, J. Med. Chem. **51**, 6876 (2008).

108. E. Fanizza, R. M. Iacobazzi, V. Laquintana, G. Valente, G. Caliandro, M. Striccoli, A. Agostiano, A. Cutrignelli, A. Lopedota, M. L. Curri, M. Franco, N. Depalo, and N. Denora, Nanoscale **8**, 3350 (2016).

109. A. Lopalco and N. Denora, in *Methods Mol. Biol.* (Humana Press, New York, NY, 2018), p. 347.

110. N. Depalo, M. Corricelli, I. De Paola, G. Valente, R. M. Iacobazzi, E. Altamura, D. Debellis, D. Comegna, E. Fanizza, N. Denora, V. Laquintana, F. Mavelli, M. Striccoli, M. Saviano, A. Agostiano, A. Del Gatto, L. Zaccaro, and M. L. Curri, ACS Appl. Mater. Interfaces **9**, 43113 (2017).

111. K. Sun, Z. Gao, Y. Zhang, H. Wu, C. You, S. Wang, P. An, C. Sun, and B. Sun, J. Mater. Chem. B **6**, 5876 (2018).

112. H. J. Kwon, M. Y. Cha, D. Kim, D. K. Kim, M. Soh, K. Shin, T. Hyeon, and I. Mook-Jung, ACS Nano **10**, 2860 (2016).

113. N. D. Donahue, H. Acar, and S. Wilhelm, Adv. Drug Deliv. Rev. In Press (2019).

114. J. R. Melamed, S. A. Ioele, A. J. Hannum, V. M. Ullman, and E. S. Day, Mol. Pharm. **15**, 5135 (2018).

국 문 초 록

암 세포뿐만 아니라 다양한 주변세포와 종양 관련 인자들의 복잡한 구성으로 조직된 종양미세환경은 암의 진단과 치료에 있어 핵심 요소로 자리잡고 있다. 따라서 종양 미세환경의 근본적인 이해를 돕기 위한 복합 영상 조영제의 개발이 절실히 요구되고 있다. 본 연구에서는 산화철 기반의 다중 복합 조영제의 제조와 표면처리 방법을 연구하고 이를 종양 미세환경의 정밀 영상 획득에 응용하고자 하였다.

첫번째 파트(챕터 1)에서는, 근적외선 형광을 띄는 실리카로 코팅된 초상자성 산화철 나노입자 (NF-SIONs)의 제조 방법과 동소 뇌종양 모델에서의 종양 관련 대식세포 특이적섭취에 대해 다루었다. NF-SIONs 는 reverse microemulsion 방법으로 제조되었으며, 두 단계의 연속된 실란화 공정을 통해 Cy 5.5 형광염료와 폴리에틸렌글리콜의 동시 도입을 가능케 하였다. 이렇게 합성된 NF-SIONs 는 뛰어난 분산 및 형광 안정성과 함께 생체 적합성을 갖는 것으로 확인되었고, 면역형광염색 분석 결과, 체내 주입된 NF-SIONs 가 뇌종양 세포 및 정상 뇌조직 세포들에 비해 종양 관련 면역세포들에 더욱 많이 섭취되었음이 확인되었다.

두번째 파트(챕터 3)에서는, 폴리에틸렌글리콜로 기능화된 산화철 나노입자에 다기능성을 추가적으로 부여하기 위한 방법으로 가지 구조의 리간드를 표면에 도입하는 방법에 대해 다루었다. 가지 구조 리간드 말단의 아민 결합자리에 NHS-ester 로 말단이 활성화된 Cy 5.5 형광염료와 뇌종양 바이오마커로 알려진 Translocator protein 18 kDa (TSPO)를 표적하는 리간드 (CB 235)를 동시에 첨가하여 결합하였다. 또한 TSPO 를 표적하는 경쟁적 저해제를 먼저 주입함으로써, 체내 주입된 나노입자가 종양 주변에서 갖는 TSPO 특이적 거동을 평가하였다.

본 학위논문은 종양 모델에서의 체계적인 면역 형광 분석을 통해, 기능화된 산화철 나노입자의 합성과 종양 정밀 영상화로의 응용연구를 다루었으며, 도출된 연구결과들을 바탕으로 난치성 암의 치료 향상에 기여할 것으로 기대된다.

주요어: 산화철 나노입자, 형광 표지, 가지 구조 리간드, 종양 미세환경, 종양 관련 대식세포, 다중 암 영상

학번: 2012-22451